

***Understanding the effect of process-induced porosity on the
localized corrosion 316L stainless steel manufactured by laser
powder bed fusion***

by

Mariela Calizaya Chipana

*A thesis submitted for the degree of
Master of Professional Engineering in Chemical Engineering
May 2023*

Abstract

The wide adoption of Laser Powder Bed Fusion (LPBF) in additive manufacturing has led to the need for a comprehensive understanding of the corrosion behavior of LPBF-fabricated components [1]. This thesis focuses on the pitting corrosion behavior of 316L stainless steel, emphasizing the influence of process-induced porosity. The impact of various defects on pitting corrosion behavior was explored through a series of experimental investigations using cyclic potentiodynamic polarization in a 0.6M NaCl solution.

The study revealed that LPBF 316L SS exhibited superior pitting resistance compared to its wrought counterpart [2]–[7], even in the presence of manufacturing defects. Interestingly, despite their larger size and open porosity, gas voids were not the preferred sites for pitting propagation. The presence of these voids did not accelerate the accumulation of metal cations, thus diminishing their impact on pitting corrosion. Instead, other defect types, such as lack of fusion (LOF) porous and microcracks, demonstrated a preference for pitting initiation and propagation. However, the size of LOF did not significantly affect the pitting resistance, suggesting other factors play a more substantial role. Notably, the presence of multiple defects significantly decreased the pitting potentials. Further research is needed to explore this underlying mechanism.

These findings provide valuable insights into the behavior of different defects and their role in pitting corrosion, contributing to developing strategies for enhancing the corrosion resistance of LPBF-fabricated components.

Keywords—Additive manufacturing, LPBF, 316L stainless steel, pitting, porosity, Cyclic potentiodynamic polarization, Microcracks, Gas voids, Lack of fusion (LOF).

Mariela Calizaya Chipana
38 Pitt Street, Saint James WA

17.05.2023

A/Prof Hari Vuthaluru

Associate Professor in Minerals, Energy and Chemical Engineering School

Curtin University

Kent Street, Bentley

GPO Box U1987 Perth WA 6845

Dear A/Prof Hari Vuthaluru

I, Mariela Calizaya Chipana, hereby submit my thesis entitled “Understanding the effect of process-induced porosity on the localized corrosion 316L stainless steel manufactured by laser powder bed fusion” as part of my requirements for completion of the degree of Master of Professional Engineering in Chemical Engineering.

I declare that this thesis is entirely my own work with the exception of the acknowledgements and references mentioned.

Yours sincerely,

Mariela Calizaya

Mariela Calizaya Chipana

20400648

Declaration of published work

I acknowledge that parts of the progress report presented at the end of the first semester of this project have been used in the following chapters of this thesis, and the report has been properly referenced:

Abstract

Chapter 1. INTRODUCTION

Chapter 2. LITERATURE REVIEW

Chapter 3. EXPERIMENTAL SETUP

Chapter 4.. RESULTS

Chapter 5. CONCLUSIONS

References

Acknowledgments

I desire to extend my heartfelt appreciation to my thesis supervisor, Dr. Ke Wang, for his exceptional guidance, outstanding leadership, and ongoing support during the development of this study. Dr. Wang's deep knowledge of the corrosion area and his unwavering guidance and profound insights have played a pivotal role in shaping the success and refinement of this thesis.

I am also deeply grateful to my beloved family, my father, Gregorio Calizaya, my mother Maria Vilca, my beloved sisters Rosalia and Luisa Calizaya. Their unwavering support and encouragement throughout this research journey have meant the world to me. Their belief in me and their constant motivation provided me with the strength and determination to overcome challenges and pursue excellence in my work. I am truly thankful for their understanding and patience during the times when I needed to dedicate long hours to this project.

Additionally, I would like to extend my appreciation to my friends, colleagues, and fellow researchers at Curtin Corrosion Centre, who have provided valuable insights, engaging discussions, and a collaborative atmosphere. Their contributions have enriched my research experience and broadened my perspective.

I am immensely grateful to everyone who has been a part of this research endeavor, and I am truly fortunate to have received such incredible support and guidance from my supervisor, family, and colleagues.

Table of Contents

1. INTRODUCTION	1
1.1. Structure of the report	3
2. LITERATURE REVIEW	4
2.1. Process-Induced Porosities	4
2.2. Mechanisms of Pitting	5
2.3. Process-Induced Porosity Effect on Pitting	9
3. EXPERIMENTAL SETUP	13
3.1. Facilities	13
3.2. Syringe cell description	13
3.3. Set up of the syringe cell	14
3.4. Samples	16
3.5. Microstructure characterization	17
3.6. Porosity characterization	18
3.7. Cyclic potentiodynamic polarization (CPP)	18
4. RESULTS	20
4.1. Microstructure Characterization	20
4.2. Cyclic polarization characteristics and pit morphology	24
5. DISCUSSIONS	31
6. CONCLUSIONS	34
REFERENCES	35
Appendix A: A photograph of the syringe cell configuration and data obtained in the experiments.	38

List of Figures

- Fig. 2.1 The schematic diagram of pit formation of LPBF 316L SS exposed to aerated chloride solution 7
- Fig. 3.1 Description of syringe cell setup 1) Method proposed by Panindre [48]. 2) An enhanced syringe cell incorporating a metal bridge. 15
- Fig. 3.2 Schematic diagram of syringe cell incorporating a metal bridge used in this experiment. 16
- Fig. 4.1 Scanning electron microscope (SEM) of LPBF 316LSS shown the microstructure of the specimens (a, b). The green arrows refers to the nano inclusions and the yellow ones refers to the cellular networks. 21
- Fig. 4.2 The defects in the 316L stainless steel (316LSS) specimens fabricated using laser powder bed fusion (LPBF) were identified using a light optical microscope (LOM). The red arrows refers to the gaps, the yellow refers to the LOF pores , the orange to the spherical porous and the green to the non-spherical porous. 23
- Fig. 4.3 Metastable pitting behavior of individual specimens in Wrought 316l stainless steel and printed specimens. 24
- Fig. 4.4 The morphology of the wrought and 316L stainless steel (316L SS) LPBF specimens before and after the test. The figure provides visual representations of the specimen surfaces, illustrating any changes in morphology due to the testing process. The comparison between the pre-test (a-b) and post-test (f-j) and images of the pit (k-o) allows for a better understanding of the structural alterations that occurred during the testing of LPBF specimens. 29
- Fig. 4.5 Correlation between potential values and porous area in tested specimens 30

List of Tables

Table 2.1 Summary of reported studies of process-induced porosity on pitting of LPBf 316L SS	12
Table 3.1 Chemical composition of specimens and powder	17

1. INTRODUCTION

The successful application of laser powder bed fusion in several industries has revolutionized additive manufacturing (AM) [8], [9]. The ability of LPBF to produce complex and customized components has opened up new avenues for design and manufacturing. However, the presence of inherent defects, such as process-induced porosity, poses significant challenges in terms of the mechanical and corrosion properties. Among the different forms of corrosion, localized corrosion, particularly pitting corrosion, stands out as a major concern due to its potential to cause premature failure.

To address this critical issue, this thesis aims to comprehensively investigate the effect of process-induced porosity on the localized corrosion behavior of 316L stainless steel fabricated using LPBF. Process-induced porosity is a common occurrence in LPBF, arising from the complex thermal and mechanical interactions during the fabrication process. Understanding the influence of process-induced porosity on pitting corrosion is vital but remains a challenging task for researchers and industry practitioners.

The existing literature presents conflicting findings on the impact of process-induced porosity on pitting corrosion behavior, contributing to a lack of consensus in this field. Moreover, many studies have neglected to consider the issue of crevice corrosion during pitting tests, leading to unreliable experimental data. Therefore, there is a significant gap in the literature concerning the experimental techniques employed to evaluate the relationship between process-induced porosity and pitting corrosion. Addressing this gap, the present study seeks to examine the hypothesis: **Does the presence of process-induced porosity in LPBF 316L stainless steel samples have a significant effect on localized corrosion behavior, specifically on pitting susceptibility, when compared to their wrought 316L counterparts?**

To test and verify this hypothesis, an enhanced syringe cell method for localized electrochemical testing of LPBF 316L stainless steel was developed in this study. This methodology integrates the advantages of the syringe cell method. By directly pressing the syringe tip against the sample surface, the enhanced syringe cell method enables the evaluation of porosity's influence on pitting susceptibility avoiding the interference by crevice corrosion. Notably, the enhanced syringe cell incorporates a metal bridge, offering precise measurements and improved control over experimental conditions, thus ensuring the integrity and reliability of the results. This original solution will provide researchers and industry practitioners with an efficient tool to study the pitting corrosion behavior of LPBF-fabricated components while accurately analyzing and obtaining reliable experimental results.

In addition to addressing the influence of process-induced porosity, the study also focuses on exploring the impact of different defect types, including microcracks, gas voids, and Lack of Fusion (LOF) defects, on the pitting corrosion behavior of LPBF 316L stainless steel. By examining these various defect types and their roles in pitting initiation and propagation, the study contributes to a more comprehensive understanding of defect-related corrosion mechanisms in LPBF-fabricated components.

By leveraging these outcomes, the study not only fills gaps in the current literature but also paves the way for future research endeavors. The enhanced syringe cell method, the focus on active porous regions, and the utilization of cyclic potentiodynamic polarization testing collectively contribute to a specific understanding and to the development of more effective corrosion control strategies for LPBF-fabricated components. Furthermore, the investigation of different defect types adds an additional layer of originality to the study, shedding light on their specific contributions to pitting corrosion behavior. This understanding of defect-

related corrosion mechanisms can inform future design and optimization processes, leading to enhanced corrosion resistance in LPBF applications.

1.1. Structure of the report

The introduction highlights the importance of understanding this effect in ensuring the integrity of LPBF-produced components. The chosen solution, the syringe cell method, is justified as a convenient alternative to traditional electrochemical tests. The experimental methodology chapter describes the manufacturing of samples, microstructure characterization techniques, and the cyclic potentiodynamic polarization method. The results and discussions chapter presents findings on the presence of defects and their influence on pitting corrosion behavior. The thesis concludes with implications for optimizing LPBF processes and future research directions, providing valuable insights for enhancing the performance and durability of LPBF-produced stainless steel components.

CHAPTER 2

2. LITERATURE REVIEW

2.1. Process-Induced Porosities

More recently, technological innovation has driven novelties that promote reduced manufacturing time and higher-quality output. One innovative approach to overcome these challenges is additive manufacturing (AM) technology, also known as 3D printing [8], [9]. AM technology offers substantial benefits over traditional casting, rolling, and forging methods. Besides that, this technology is employed but is not limited to aerospace, automotive, and medical applications, allowing the fabrication of items with geometric complexity that traditional manufacturing methods merely cannot [1]. As a result, this technology is gaining traction, with faster manufacturing cycles and more lasting customized parts. Despite their benefits, AM technology has shortcomings, such that 3D printers and metal powders are costly and do not allow for the production of extremely massive parts [8]. Nonetheless, this technique still has significant advantages that eventually exceed its drawbacks [10].

The most well-known and extensively used additive manufacturing method is laser powder bed fusion (LPBF). Its widespread application is because it generates 316L stainless steel with higher qualities than its predecessors. This method combines metal powder particles with a heat source, a laser, or an electron beam to create components with geometric intricacies. However, the laser powder bed fusion (LPBF) technique inevitably produces components with porosity. Thus, manufacturing without porosity remains difficult despite recent breakthroughs in porosity reduction [1].

The intense thermo-mechanical process of manufacturing LPBF produces distinct microstructures with high heterogeneities [8]. One of these defects is the porosity, which

owes its intrinsic characteristics to the energy density of the laser. The localized capture of evaporation products can cause porosity formation from the highly dynamic melt pool during the melting and solidification process [11] or lack of fusion (LOF) [12]. Hence, the emergence of manufacturing defects in producing this material still affects the quality of LPBF 316L SS [8]. Indeed, the related industry has acknowledged this issue. Thus, understanding how process-induced porosity affects the development of LPBF 316L SS pitting corrosion is vital and remains challenging [4], [10]. In principle, the pores in LPBF 316L SS specimens may be divided into spherical and non-spherical. Spherical pores, in general, are often smaller than irregular-shaped pores. The major cause of the formation of spherical pores is gas trapped inside the powder material or the melt pool. Hence, a common denominator is the presence of spherical pores in LPBF-produced specimens, regardless of the manufacturing parameters utilized to create them. Because of their spherical form, this kind of pores have a less negative influence on localized corrosion [3]. Irregular pores due to lack of fusion (LOFs) are typically formed when inappropriate parameters are used during partial powder melting occurs, resulting in a drop in the density of the material.

2.2. Mechanisms of Pitting

Pores are a common issue with LPBF components. Porosity and fractures are ideal corrosion sites formed by their particular microstructures and inner flaws [3], [7], [13]–[16]. At high anodic potentials, the pores act as pit nucleation sites, negatively affecting the passive layer and leading to metastable pitting. Corrosion mechanisms in LPBF 316 LSS are somehow similar to its predecessor 316L SS; both have a primary barrier of chromium oxide film (Cr_2O_3) on their surface because of the presence of high chromium in the alloy [17]. However, although the pitting mechanism should be the same, it is still unclear how porosity will influence the pitting corrosion.

Additionally, porosity can hinder the mass transport process inside the porosity cavity, which facilitates the stability of pit propagation [4], [18]. Like porosity, surface roughness caused by AM technology processing can also affect pitting behavior [19]. Hence, considerable efforts have been made to broaden knowledge about pitting corrosion mechanisms in pores. Thus, understanding the pitting corrosion mechanisms induced by pores is crucial to develop effective prevention and mitigation strategies.

Previous research by Duan et al. [9] has shed light on the mechanism of pitting corrosion in pores, emphasizing the role of the oxide film's composition and the local environment on pit formation and growth. Hence, it is essential to consider pitting corrosion in wrought 316 LSS as a benchmark to understand the pitting mechanism induced by gas pores.

In general terms, Pitting corrosion occurs when this protective oxide film breaks down, allowing the bare metal direct environmental exposure. Any composition modifications to the oxide film can influence pit formation and a pit nucleation site [18], [20], [21]. Pitting corrosion is developed in three stages: nucleation, metastable pitting, and stable pit development. This classification provides guidelines for understanding the two important mechanisms that rule the pitting process: nucleation and the transition from metastable to stable pit growth [17], [22]. The nucleation of pitting corrosion occurs when the passive layer is damaged due to the exposition of aggressive cations concentration and microstructural defects such as porosity [4]. As the pit nucleates, the conditions within the pit must maintain active metal dissolution for the pit to transition from metastable to stable [23]–[25].

In a schematic diagram, **Fig. 2.1a** depicts the pitting mechanism induced by the manufactured gas pores of SLM 316L SS. Here metal M has a spherical shape representing

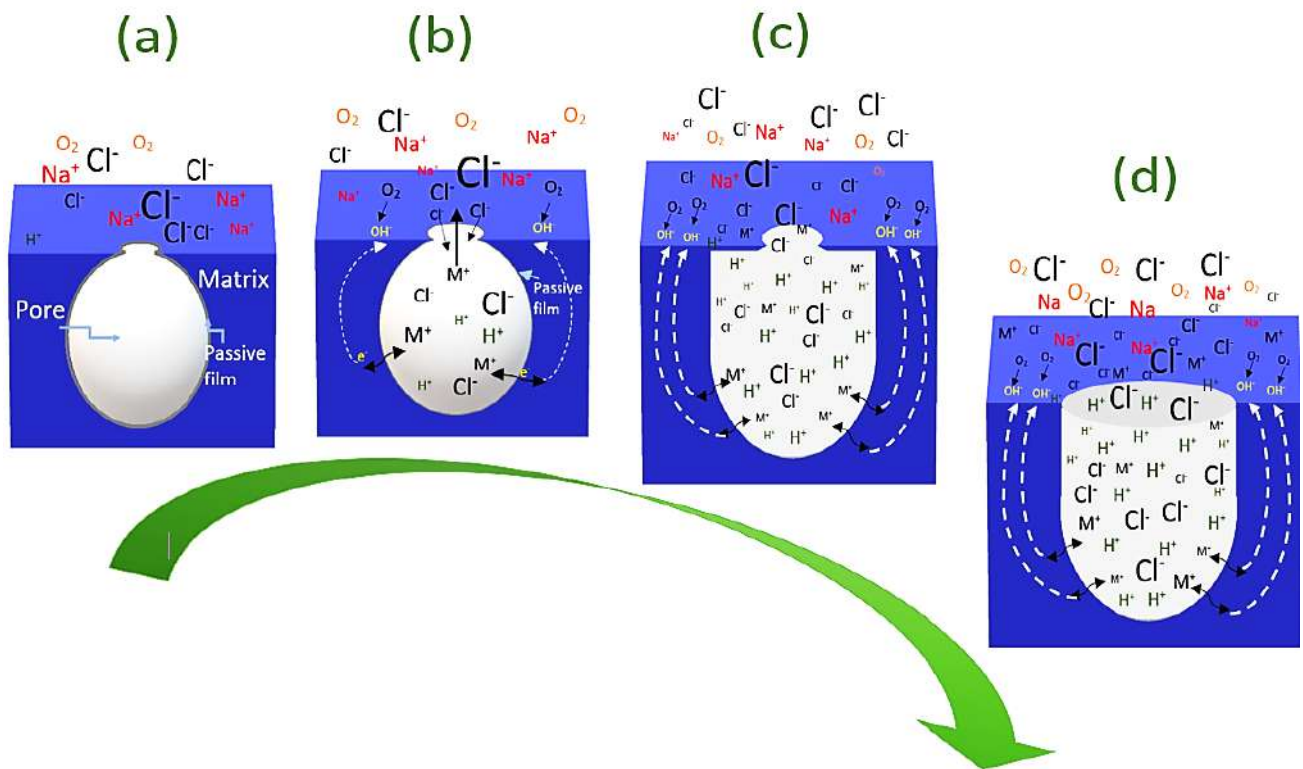


Fig. 2.1 The schematic diagram of pit formation of LPBF 316L SS exposed to aerated chloride solution

an open gas pore immersed in an aerated sodium chloride solution. Inside the pores, rapid metal dissolution occurs. In contrast, oxygen reduction occurs on adjacent surfaces, which causes the migration of chloride ions Cl^- towards the pore to balance the charge and hold electroneutrality [26], [27]. The aggressive environment inside the pore contains an excess, mainly of chloride and metal cations (Cl^- and M^+). The accumulation of the hydrogen ion H^+ inside the pit is derived from the metal cations hydrolysis. The cations concentration at the pit surface is utilized to determine the severity of the electrolytes inside the pits. Once the metal cation is higher than the critical value, the pit propagation will be maintained [24]. Electrochemical reactions are linked to the cation's concentration in SLM 316L SS. These dynamic processes occur on the surface and interior pit, where metal cations diffuse toward the bulk solution (**Fig. 2.1b**).

The gas pore does not have a corrosive environment initially, allowing a passivating layer to grow on the pore. Furthermore, the passive film always tries to keep an equilibrium state

of dissolution and renewal [18]. At this stage, the passive layer disintegrates inside the pore due to electrochemical dissolution generating cations. During this process, the gas pores have a faster rate of dissolution of the passive layer and a slower rate of diffusion than adjacent surfaces (since now named matrix) [26].

Hence, the concentration of metal cations and the electrochemical breakdown of the pore's passive layer would initiate pitting corrosion within the pore. On the other hand, the solubility of oxygen in concentrated solutions is nearly negligible, resulting in no oxygen reduction inside the pit [26]. Pitting, cathodically speaking, preserves the remains of the metal surface because oxygen reduction in the matrix tends to prevent corrosion. The local pH inside the pores hence drops at this stage, which triggers a decrease in the thickness of the passive layer [28], [29]. The thinning of the passive film may affect the pace of film disintegration and cation diffusion in the gas pore. So, the pace of passive film disintegration increases when the metal cations also rise.

Furthermore, the passive film thickness is the nano-scale size, meaning that its passive film thickness is three to four orders of magnitude less than the pit size. Moreover, like with film breakdown, the rate of metal cation transport increases with cation accumulation. As the pH decreases to the critical value, the build-up rate of metal cation within the gas pore accelerates. At this moment, the thickness of the passive film decreases and finally vanishes (**Fig. 2.1c**). Additionally, inside the pore, the predominant dissolution occurs in the active state metal, surpassing the dissolution of the passive layer. As a result, metal cation build-up relies on active matrix dissolution and metal cation mass transport [4], [26], [28], [29].

As illustrated in **Fig. 2.1d**, the active state dissolution increases the transfer between the gas pore and the matrix with or without cover. According to the pitting corrosion framework provided by Frankel *et al.* [17], ongoing pit formation occurs when the active dissolution rate is more major than the diffusion rate in the matrix, maintaining so the cation

concentration in the pit. Stable pitting corrosion thus starts when cation concentrations at the pit surface reach critical levels. As a result, when the covered gas pore reaches the critical concentration of the metal, the cover rupture starts. If metal concentration can sustain active dissolution after the passive film is entirely torn, the pit will reach metastability and transition to stable growth; otherwise, it will re-passivate [4].

2.3. Process-Induced Porosity Effect on Pitting

Different studies used cyclic potentiodynamic polarization (CPP) to better understand metastable pitting behavior. Consequently, two study groups [30], [31] compared the corrosion behavior of LPBF 316L versus wrought samples in 0.6 M sodium chloride solution. A discrepancy is given between researchers and provided unexpected findings, demonstrating that although being assessed under the same conditions, The CPP curves produced in both experiments in LPBF 316L samples and their conventional counterpart present distinct outcomes. For example, Chao *et al.* [30] found that LPBF 316L samples have a greater breakdown potential for pitting than their conventional predecessor, whereas Nie and colleagues [31] indicates the contrary.

These findings suggest that the performance of LPBF against pitting corrosion is not only attributable but also to its cellular properties [8], [32], [33]. Thus, after thoroughly analysing the literature, we discovered the same results as previously reported. In fact, some studies [3], [30], [34] found that specimens of 316L printed by laser powder bed fusion (LPBF 316L) had stronger corrosion resistance than wrought 316L, but others [7], [31], [35], [36] found lower corrosion performance. Another important finding found was that the test electrolyte affects the corrosion resistance of LPBF. Higher concentrations of NaCl, for example, supply more Cl⁻ ions to attack; hence, they might predict lesser corrosion resistance than lower concentrations of NaCl electrolytes.

Furthermore, several researchers [3], [30], [34], [37] concur that the LPBF-316L process prevents the production of manganese sulphide (MnS) inclusions. As a result, in theory, the LPBF-316L has better corrosion resistance. Even so, LPBF-316L, unlike its predecessors, which feature MnS inclusions and are the primary cause of pitting corrosion, still needs to show an improved corrosion performance. Therefore, the lack of this inclusion in LPBF specimens does not explain why they do not have a good pitting corrosion performance. Although MnS inclusions are the main contributor to pitting corrosion, it is important to note that pitting corrosion is also affected by pores, grain size, and inclusions, among other factors. To reinforce this notion, Wang *et al.* [38] revealed that porosity influences the performance of the material under consideration. They proposed that subsurface pores, rather than surface pores, served as active pitting corrosion sites. Also, they claimed that the extreme thermodynamic changes made during the process caused a considerable stress concentration around the closed subsurface pores, making them susceptible to pitting corrosion. Moreover, corrosion resistance can be judged using the CPP charts. A higher potential for pitting (E_{pit}), corrosion (E_{corr}), and re-passivation (E_{rp}), as well as a low corrosion current density (i_{corr}) and a low frequency of metastable pitting, indicate the highest corrosion resistance.

Sander *et al.* [3] proclaimed that the pitting potential in LPBF 316L samples at 0.584 wt% NaCl is greater than in wrought SS 316L specimens. According to their idea, inclusions were refined or deleted throughout the LPBF process, reducing the number of pit nucleation sites in LPBF-316L samples. They also ruled out porosity's influence because their experiments show that the porosity samples were between 0.01 vol.% and 0.4 vol.% and how porosity influences the potential of pitting corrosion. Furthermore, their findings reveal that the porosity% of the LPBF 316L samples does not affect the E_{corr} , E_{pit} , and i_{corr} potentials when compared with their counterpart. In contrast, Sun *et al.* [7] evaluated LPBF 316L specimens

at 0.9 wt% NaCl solutions with vol.% porosities greater than 1.7% founding a drop in E_{pit} and an increase in i_{corr} as vol% porosity increased. This study exposed a slightly greater passive current density in LPBF-316L specimens than in wrought SS316L specimens for the specimens studied. It reveals, therefore, that the corrosive behavior of LPBF 316L and its precursor is nearly the same in both samples and that porosity has little effect on resistance to localized corrosion. However, Ziętała *et al.* [15] detected a lower E_{corr} in the 316LSS specimens created by laser engineering net modeling (LENS) using the same 0.9% NaCl electrolyte but a different fabrication technique.

Furthermore, Laleh *et al.* [2] confirmed the impact of porosity on corrosion potential in their studies at 3.5 wt% NaCl concentrations. It is due to the LPBF 316L specimens producing lower E_{pit} in the lower density (high porosity) samples. Moreover, their findings suggest that the pore properties of the LPBF 316L samples play a crucial role in limiting pitting corrosion susceptibility. On the other hand, Trelewicz and colleagues [33] found that specimens at 0.1 M LPBF 316L HCL concentration exhibited decreased passivity. However, the results are distinct from the typical polarization behavior at this concentration reported by other researchers [39], [40], which is likely that these results have been affected by crevice corrosion.

Furthermore, studies [3], [7] pointed out a decrease in E_{rep} as porosity increased in LPBF specimens at concentrations of 0.584 and 0.9 wt% NaCl. As a result, once stable pitting developed, the sample with increased porosity lost its ability for re-passivation. Similarly, these results displayed that the re-passivation potential is important when evaluating corrosion behavior in LPBF specimens. Sander *et al.* [8] also indicated that samples with high porosity stand superior metastable pitting frequency. They also suggested that the fine pores in the sample generate metastable pitting. Vukkum *et al.* [32], on the other hand, indicated that they did not find pores surrounding metastable pits in LPBF-316L specimens

exposed to 3.5 wt% NaCl concentration. Thus, **Table 2.1** summarizes the findings from the literature about process-induced porosity in LPBF 316L SS pitting.

Table 2.1 Summary of reported studies of process-induced porosity on pitting of LPBF 316L SS

No	Electrolyte	Ref. Electrode	Specimens' preparation for Potentiostatic testing	Summary	Ref.
1	0.584 wt% NaCl	SCE	The specimens were flush-mounted in epoxy. To avoid crevice corrosion, the interface was lacquer-insulated. Method used: Three-electrode electrochemical cell.	The LPBF 316L corrosion performance was higher than wrought 316L. The LPBF-316L porosity has a negative impact on re-passivation potential but not on corrosion potential.	[3]
2	0.9 wt% NaCl	SCE	This report did not detail enough about the pre-preparation of the specimen. Method used: Three-electrode electrochemical cell.	The LPBF 316L corrosion resistance was lower than wrought 316L.	[7]
3	3.5 wt% NaCl	SCE	This report did not detail enough about the pre-preparation of the specimen. Method used: Three-electrode electrochemical cell.	Porosity has an unfavorable impact on LPBF 316L corrosion performance.	[5]
4	3.5 wt% NaCl	Ag/AgCl	The specimens were cold-mounted in an epoxy resin. Method used: Three-electrode electrochemical cell.	The LPBF316L corrosion performance was not impacted by micropores but was harmed by lack-of-fusion pores.	[2]
5	3.5 wt% NaCl	SCE	The samples were welded together using copper wire before being immersed in epoxy resin. The edges of the samples were covered with nail polish to avoid crevice corrosion. Method used: Three-electrode electrochemical cell.	Although porosity% negatively influenced corrosion performance, LPBF 316L performed better than wrought 316L.	[6]
6	Range 0.01M-3.0M NaCl	SCE	The samples were embedded in epoxy resin. Method used: Three-electrode electrochemical cell.	At different NaCl solution concentrations, the LPBF 316L corrosion performance outperformed wrought 316L corrosion resistance. However, in very acidic environments, the LPBF-316L porosity has lesser corrosion resistance.	[4]
7	0.1M HCl	Ag/AgCl	This report did not detail enough about the pre-preparation of the specimen. Method used: Three-electrode electrochemical cell.	LPBF316L has a lower corrosion performance than wrought 316L. However, the results shown in this work differ from the normal polarization published by other researchers in similar contexts [39], [40]; this polarization response might be altered by crevice corrosion.	[33]

CHAPTER 3

3. EXPERIMENTAL SETUP

3.1. Facilities

The present study followed an experimental approach, that was developed in the Curtin Corrosion Centre.

3.2. Syringe cell description

The experiments were performed utilizing a syringe cell for conducting local electrochemical testing. This method was preferred because it can locally evaluate the porosity effect on pitting susceptibility with avoiding crevice corrosion. Based on the literature review beforementioned, it is observed that the typical electrochemical tests used entail significant errors. In many LPBF-316L experiments, it is well-recognized that crevice corrosion may substantially interfere with pitting measurement. Indeed, most passive metals that pose shallow crevices are more prone to crevice corrosion [41], [42] and are often affected by this type of corrosion before pitting corrosion. As a preventive effort, the ASTM G150-13 standard specifies a series of recommendations to limit the corrosivity in the contact area of the sample and the joints. However, these recommendations frequently include additional procedures that could be more time-consuming and complicated.

It is worth noting that the well-accepted method for avoiding crevice corrosion during pitting tests, such as the Avesta Cell [2]–[7], [33] recommended by ASTM G150, is not suitable for local electrochemical tests involving pores. Similarly, the half-immersion method also has the same disadvantage [43]. Some researchers thus attempted to avoid crevice corrosion by passivating the metal coupon before testing [44]. However, corrosion can still occur if the test solutions are excessively severe.

As a result, the syringe cell is one of the most convenient methods that minimize the drawbacks mentioned above. The setup of the syringe cell method (**Fig. 3.1-1**) includes the following features: test solution, reference electrodes, and counters. By pushing the tip of the syringe against the sample surface, direct contact of the electrolyte with the sample surface in a precise spot for electrochemical signal data (**Fig. 3.1-1b,c**). This approach, however, has practical constraints, such as the influence of capillary size on current restriction, leakage, or microcapillary tip obstruction [45], [46]. Hence, to prevent this sort of issue, the tests were performed using a short period of potentiodynamic scanning. This approach helps mitigate the potential impact of droplet size fluctuation between the test surface and syringe tip over time, which could be caused by factors such as evaporation or another characteristic [47], particularly when operating at room temperature.

3.3. Set up of the syringe cell

The experimental setup for this study involved modifying the methodology proposed by Panindre et al.[48] as indicated in **Fig. 3.1-2**. In **Fig. 3.1-1b**, the reference electrode was used directly, which increased the syringe weight and made the control of waterdrop at the barrel tip difficult. Additionally, considering the recommendations made by Choudhary *et al.* [49], contamination of the test solution often encountered when using porous frits or salt bridges. Thus, a metal bridge of platinum was introduced, effectively eliminating the risks and issues and ensuring the integrity and reliability of the experimental results [49]. A schematic diagram of the syringe cell used in this work is shown in **Fig. 3.2**.

To assemble the syringe cell setup, a standard 60 mL syringe was selected as the primary component. The syringe plunger was filled with a solution of 0.6 M NaCl, including the counting electrode (CE) and the metal bridge punched into the rubber plunger gasket **Fig. 3.1-2a**. The syringe barrel was positioned close to the electrochemical cell, as illustrated **Fig. 3.1-2c**. A Silver/Silver chloride (sat. KCl) electrode (SSC) was used as the reference

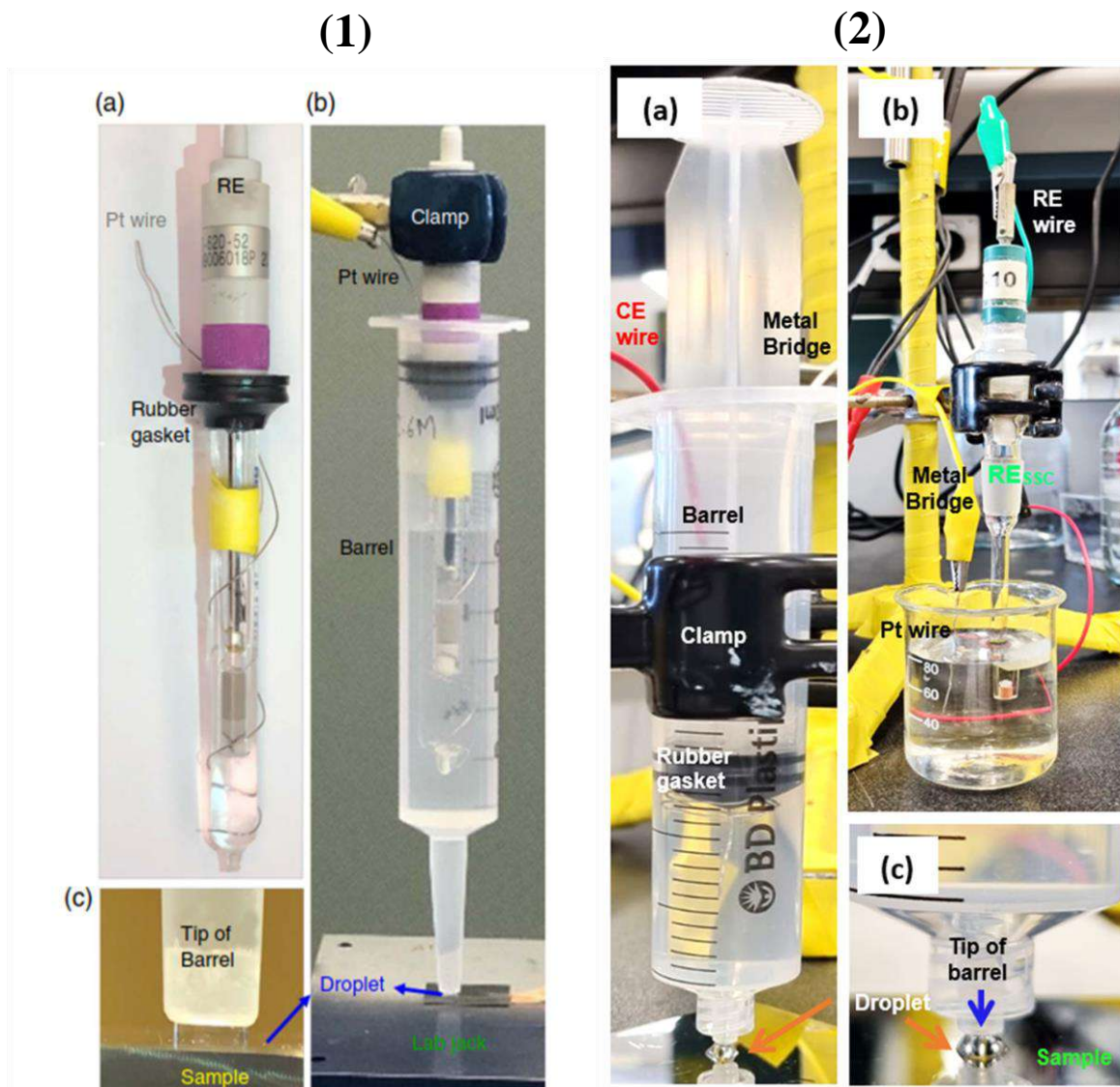


Fig. 3.1 Description of syringe cell setup 1) Method proposed by Panindre [48]. 2) An enhanced syringe cell incorporating a metal bridge.

electrode (see **Fig. 3.1-2b**), and a copper wire was soldered to the back of the specimen to establish electrical contact, **Fig. 3.2**.

To prevent the displacement of the reference electrode plunger due to its weight, the syringe's reference electrode and barrel were securely clamped in a vertical position, as depicted in **Fig. 3.1-2a,b**. This clamping ensured stability and maintained the position of the syringe setup throughout the experiment. The test sample was carefully lifted until it contacted a droplet, ensuring that the local area with porosity was exposed to the fluid within

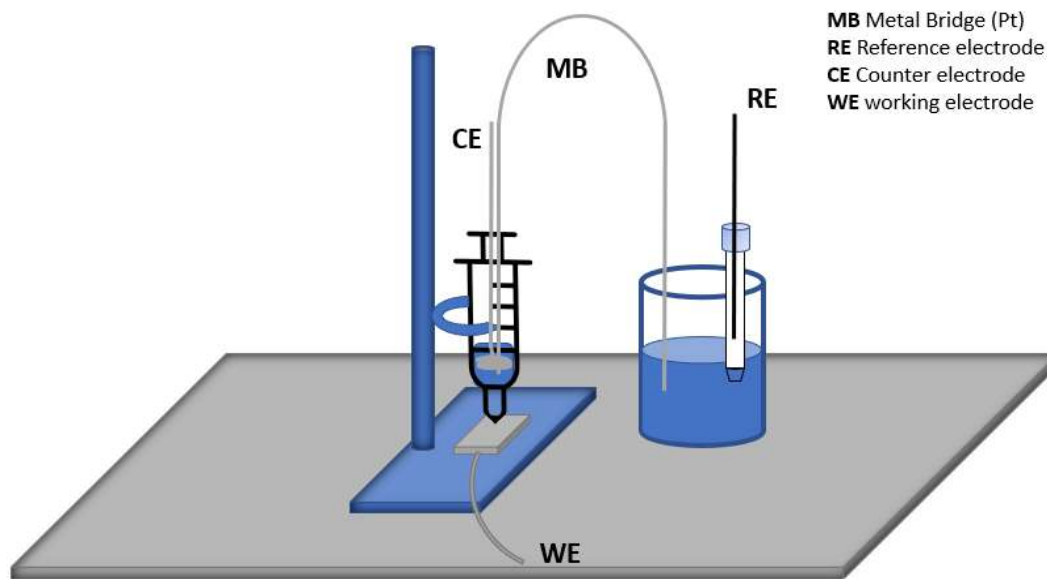


Fig. 3.2 Schematic diagram of syringe cell incorporating a metal bridge used in this experiment.

the syringe cell. To ensure accurate analysis and prevent overlapping metastable pitting events, the test area was carefully selected based on the inner diameter of the syringe tip. This resulted in an exposed test area of approximately 5 mm^2 . By focusing on this specific area, the study was able to obtain reliable data and minimize potential interference from adjacent regions.

3.4. Samples

The LPBF 316L SS samples were manufactured using the 3D system Pro X† DMP 320 with specific process parameters, including a laser power of 250 W, a scanning speed of 900 mm/s, and a layer thickness of $30 \text{ }\mu\text{m}$. The 316L powder utilized in the SLM process was supplied by TLS Technik GmbH & Co., Germany, with a particle size ranging from 10 to $45 \text{ }\mu\text{m}$.

For comprehensive analysis, the LPBF 316L SS samples were compared to their wrought 316L counterparts, which exhibiting specific chemical compositions as presented in **Table**

3.1. To enable clear identification and differentiation of the various sample types used in the experiments, a systematic naming convention was implemented. The wrought type 316L SS samples were designated with the prefix "W," while the LPBF 316L SS samples were labeled with the prefix "P" followed by a sample number. Additionally, an area designation was employed to specify the region of interest within each sample. For instance, the designation "PS4.1" indicated a printed 316L SS sample, specifically the fourth sample treated, with area 1 representing the designated region of interest. This consistent naming convention greatly facilitated effective communication and enhanced the overall understanding of the experimental findings.

Table 3.1 Chemical composition of specimens and powder

Type	Chemical composition, %wt.							
	C	Mn	Si	P	S	Cr	Mo	Ni
316L Wrought	0.02	1.66	0.42	0.03	0.03	16.70	2.14	10.07
316L Powder	0.02	1.00	0.51	0.00	0.51	17.50	2.30	11.10

3.5. Microstructure characterization

The microstructure characterization of the specimens, measuring 40 x 40 x 3 mm, involved a series of preparation steps for various microscopy techniques. For backscattered Scanning Electron Microscope (SEM) analysis, the samples underwent standard metallographic grinding and polishing procedures.

The final polishing step utilized a 0.04 µm oxide polishing suspension (OPS) obtained from Struers, Denmark. Subsequently, SEM imaging was conducted using a JEOL JSM 7800F field emission gun (FEG) SEM with an acceleration voltage of 10 kV. This high-resolution imaging technique allowed for detailed examination of the sample surfaces and visualization of microstructural features.

3.6. Porosity characterization

In addition to SEM analysis, the porosity morphologies of the samples were also observed using optical microscopy (OM). The microscope models employed for this purpose were the Nikon ECLIPSE LV150N and the Alicona IFM-G4 InfiniteFocus Microscope. The working surfaces of the samples were prepared using silicon carbide paper up to 5000 grit and subjected to ultrasonic cleaning in de-ionized distilled water, followed by cleaning with ethanol.

To quantify the porosity of the samples, image analysis software such as ImageJ was utilized. By outlining the porous regions in the images, the software's measurement capabilities were employed to accurately calculate the area of porosity.

3.7. Cyclic potentiodynamic polarization (CPP)

The cyclic potentiodynamic polarization (CPP) tests were conducted at room temperature using a Gamry electrochemical workstation (reference 600+) to investigate the porosity effect on the pit resistance. Before the CPP tests, the surface porosity morphologies were observed with LOM. The interesting areas with different type and size of porosity were marked for the subsequent CPP tests.

After the syringe cell was assembled, the test area was stabilized at open circuit potential for 1h after contacting the testing electrolyte. The CPP tests were carried out at a scan rate of 1.0 mV/s scanning the potential conducted at a scanning rate of 1mV/s from -0.02 V versus open circuit potential to 1.5 V_{SSC}, until the current reaching 100uA. The experimental test was performed at least three times to confirm the reproducibility and accurate results.

The E_{pit} was defined as the potential where stable pitting breakdown occurred, and the E_{rp} was defined as the potential during the reverse scan where the current dropped sharply. By

analyzing the results obtained from cyclic polarization tests and examining the values of E_{pit} and E_{rp} , valuable insights into the pitting corrosion behavior of different materials and porosities can be gained. Higher E_{pit} values and E_{rp} values indicate enhanced resistance to pitting corrosion.

After the completion of the CPP tests, the samples were ultrasonically cleaned in ethanol to remove any contaminants. Subsequently, the same surface area was examined using a combination of light optical microscopy (LOM). Images of the specimens were collected at various magnifications, including 5X, 10X, 20X and 50X, to capture different levels of detail.

CHAPTER 4

4. RESULTS

4.1. Microstructure Characterization

The backscattered SEM of LPBF 316L SS are shown in **Fig. 4.1a** confirms the presence of a fully austenitic single phase structure, which is in good agreement with other studies [3], [30], [33], [50]. Upon higher magnification **Fig. 4.1b** the SEM image unveils the presence of nano inclusions and cellular network dispersed throughout the microstructure. These features as indicated by arrows in **Fig. 4.1b**, consistently align with prior studies [3], [30], [51]. These nano inclusions and cellular networks can arise during the LPBF process and may have implications for the material's properties, such as mechanical strength and corrosion resistance [8], [13], [50].

Fig. 4.2 illustrates the defects observed in 316L SS LPBF specimens using a light optical microscope (**LOM**). A prominent characteristic observed in all specimens is the presence of porosity, indicating that the samples are not completely dense [7]. The defects detected include micro cracks, gaps, voids and lack of fusion pores (LOF). It is worth noting that in this area, microcracks were consistently observed, which could be formed during the solidification around the boundaries of the melt pools.

The formation of porosity and manufacturing defects are complex phenomena influenced by multiple factors, and their relative development can vary depending on the specific fabrication conditions and parameters. According to the literature, several factors such as feedstock power properties (powder particle and distribution) [52]–[55], building atmosphere [56], [57], laser input power density (LPD) [3], [12], [38], [58], laser scanning velocity (LSV) [3], [7], [59]–[62], layer thicknesses [63] and process parameters such as laser scanning strategy (LSS) [64], preheating temperature [65], and build orientation [66],

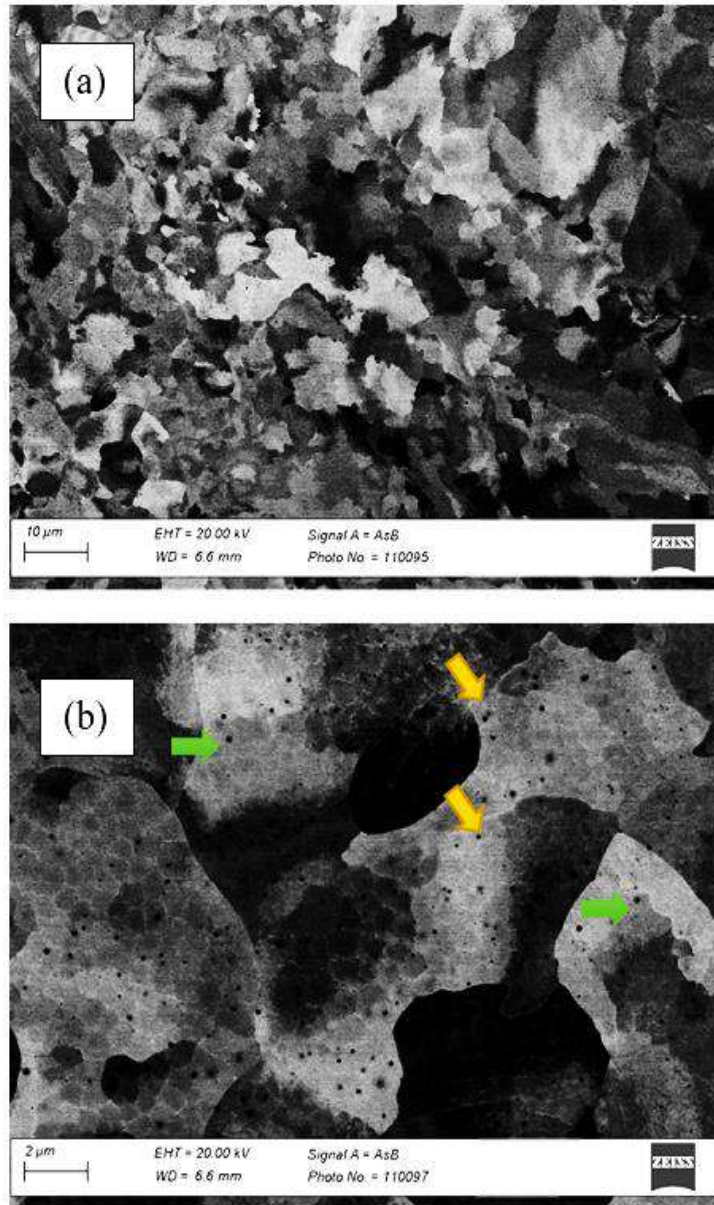


Fig. 4.1 Scanning electron microscope (SEM) of LPBF 316LSS shown the microstructure of the specimens (a, b). The green arrows refers to the nano inclusions and the yellow ones refers to the cellular networks.

[67], can influence porosity. Among the factors commonly discussed in the literature, laser power and scanning speed are commonly mentioned as critical factors affecting porosity formation. Indeed, Sander *et al.* [8] have reported that higher laser power levels and lower scanning speeds tend to result in increased porosity. Therefore, these parameters directly impact the energy input and heat transfer during the fabrication process, influencing the melting and bonding of the metal powder [3], [68], [69].

The evaluation of LOF (lack-of-fusion) porosity area, referred to incomplete fusion between adjacent powder particles and the substrate during the laser powder bed fusion (LPBF) process, revealed the presence of small balls measuring approximately 30 μm within the LOF porous regions. The presence of lack-of-fusion (**LOF**) pores, **Fig. 4.2b**, is often attributed to the application of lower LPD, resulting in penetration depth and melts pool, leading to cone-shaped melt pools. In contrast, higher LPD [38], [69], [70] and higher LSV [61], [62], [68] can cause insufficient melting, contributing to the formation of LOF pores irregular polygonal-shaped porosity at the inter-layer boundaries [12], [31], [58], [71]. Lower LPD impacts the penetration depth and melts pool, leading to cone-shaped melt pools. In contrast, higher LPD [38], [69], [70] and higher LSV [61], [62], [68] can cause insufficient melting, contributing to the formation of LOF pores.

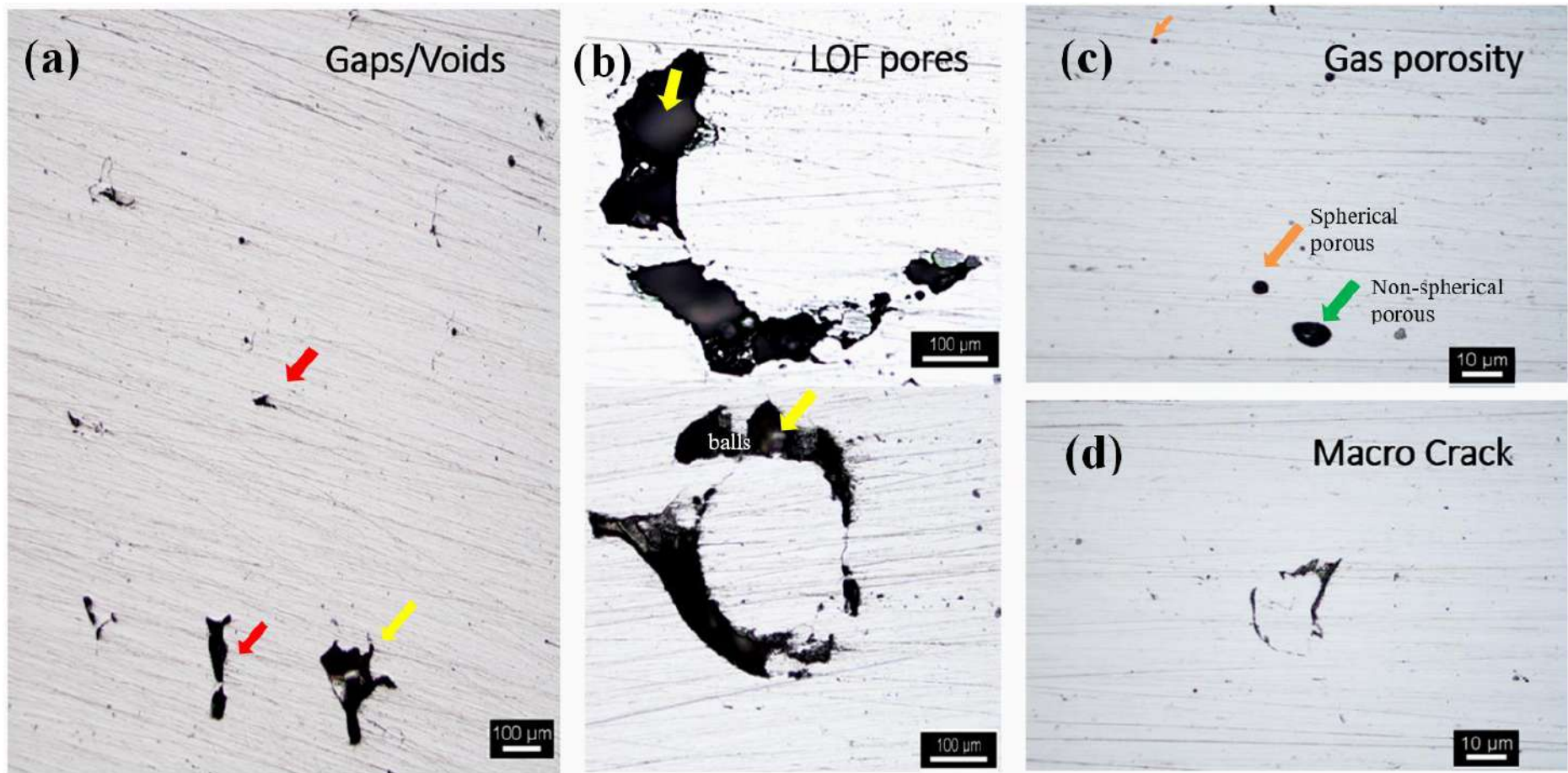


Fig. 4.2 The defects in the 316L stainless steel (316LSS) specimens fabricated using laser powder bed fusion (LPBF) were identified using a light optical microscope (LOM). The red arrows refers to the gaps, the yellow refers to the LOF pores , the orange to the spherical porous and the green to the non-spherical porous.

4.2. Cyclic polarization characteristics and pit morphology

The results of the study on the cyclic polarization characteristics and pit morphology of LPBF 316L SS with different porosities have provided valuable insights into the pitting corrosion behavior. The typical CPP curves of wrought and LPBF 316L SS are shown in **Fig. 4.3**, which exhibited self-passivation characteristics, suggesting that a passive film could spontaneously form at the surface under the conditions investigated. From the CPP curves, the pitting potential (E_{pit}) and repassivation potential (E_{rp}) were also determined. Higher E_{pit} values and E_{rp} values indicate enhanced resistance to pitting corrosion [3].

It needs to mention that the CPP curve of sample PS2.1 during the forward scan showed fluctuations, indicating the occurrence of metastable pitting. Similar behavior has been reported in both printed manufactured components [3] and their counterparts [72], [73]. The

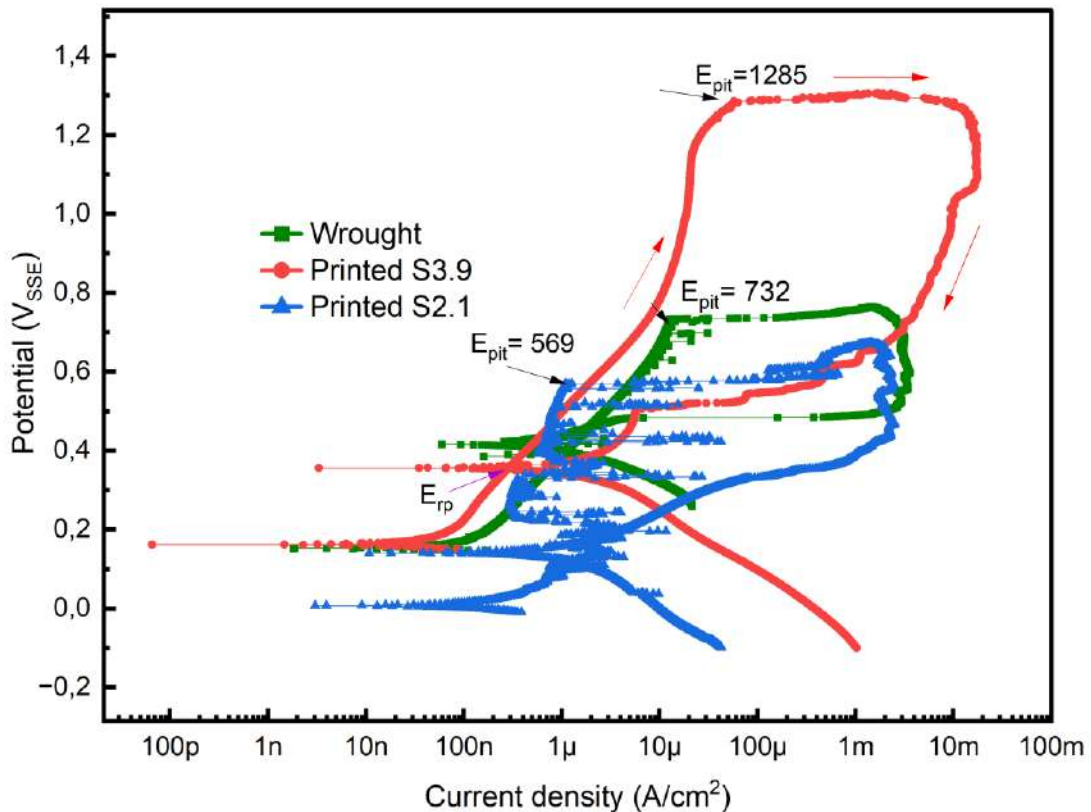


Fig. 4.3 Metastable pitting behavior of individual specimens in Wrought 316l stainless steel and printed specimens.

presence of localized defects, such as porosity, lack of fusion defects, micro cracks, voids, or other manufacturing-related factors, is considered a contributing factor to these fluctuations. These defects act as preferential sites for corrosion initiation and can lead to localized variations in electrochemical behavior.

The surface morphologies before and after CPP tests are shown in **Fig. 4.4** to illustrate the porosity effect on pitting propagation preference location. The following observations were made:

1. It was observed that pitting of LPBF 316L SS occurred at microcracks present in the samples. This indicates that microcracks serve as sites for the stable propagation of pitting corrosion. The pitting potentials measured at these microcracks were within a certain range, suggesting a consistent behavior in terms of pitting initiation.
2. Pitting was also observed at locations where lack-of-fusion (LOF) defects were present. These LOF defects provided favourable conditions for pitting corrosion to occur.
3. When both LOF and voids were present simultaneously, it was observed that pitting preferred to propagate at the LOF defects rather than at the voids. This suggests that the LOF defects play a more critical role in facilitating the localized corrosion process compared to the voids.

Overall, these results highlight the influence of different types and sizes of porosities on the pitting corrosion behavior of the samples. Microcracks and LOF defects were identified as key sites for pitting propagation of LPBF 316L SS.

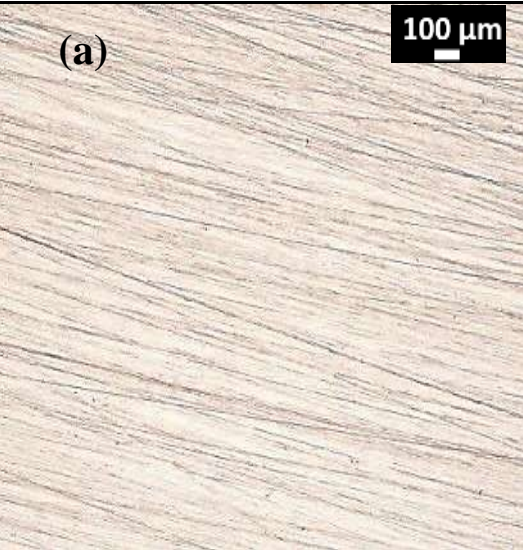
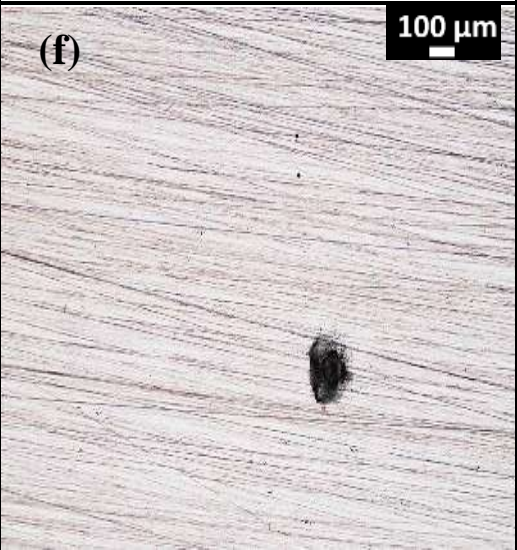
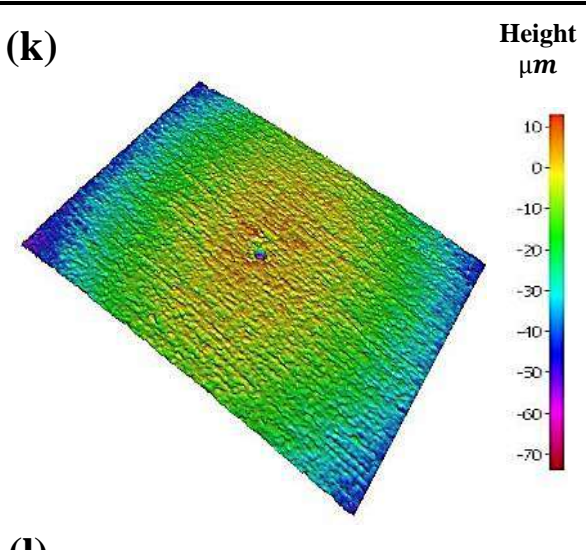
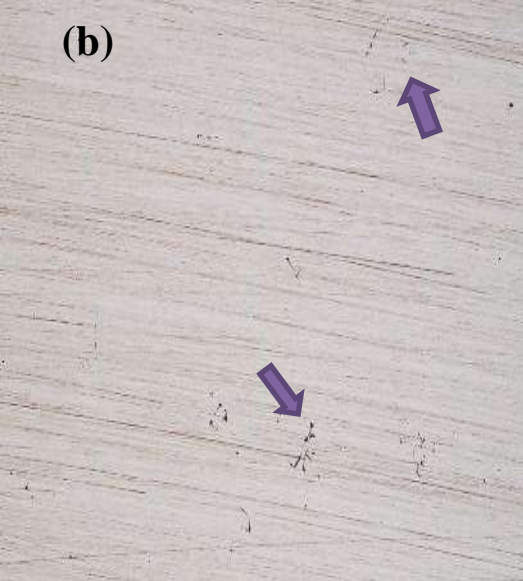
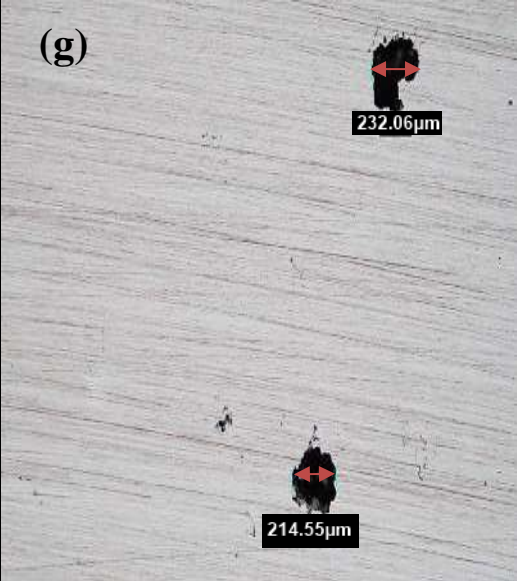
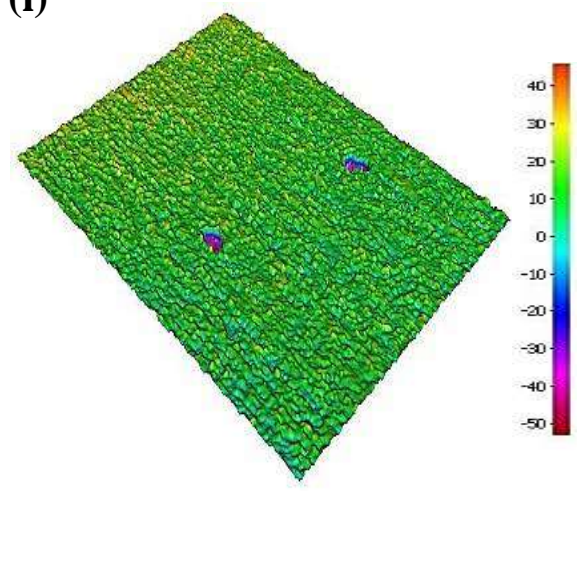
The summarized results of the pitting potentials (E_{pit}) and repassivation potentials (E_{rp}) for different types and sizes of porosities in **Fig. 4.5** have revealed interesting findings. Samples with micro cracks (PS3.2 and PS3.3) exhibited higher E_{pit} values, indicating increased

resistance to pitting corrosion compared to their 316L SS counterparts. This observation is consistent with previous literature on LPBF 316L SS [3], [30], [34], [51]. Similarly, samples with lack of fusion defects (LOF) demonstrated higher E_{pit} values than wrought counterpart, albeit slightly lower than LPBF 316L SS with micro cracks.

It is worth noting that the evaluated LOF porosities were either isolated or in close proximity to voids, as depicted in **Fig. 4.4c, d**. Additionally, it is observed that the size of lack of fusion (LOF) defects did not significantly impact the pitting potential. However, the sample with multiple defects (PS2.1) exhibited a considerably lower E_{pit} value, suggesting a heightened susceptibility to pitting corrosion, **Fig. 4.5**.

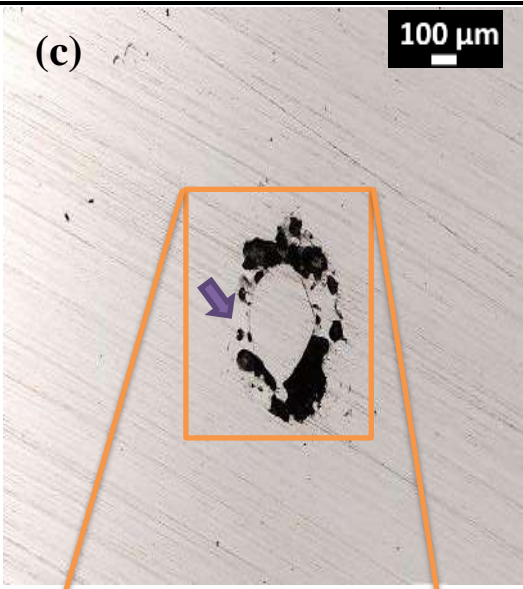
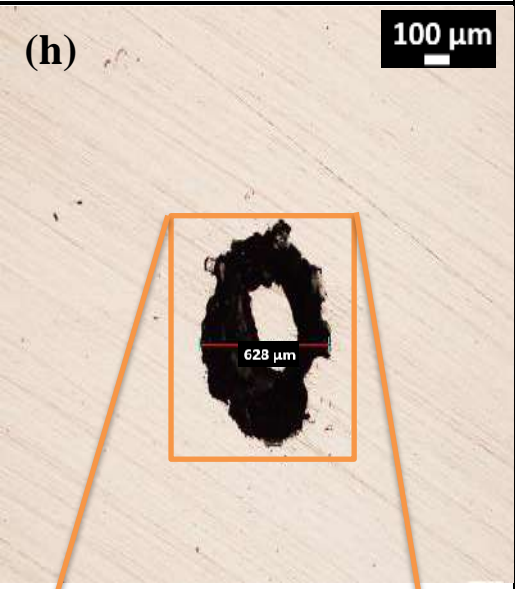
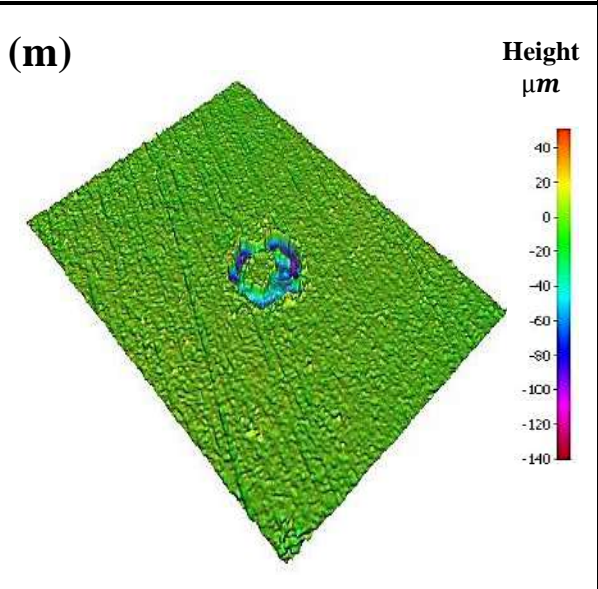
Notably, the PS2.1 sample encompassed a combination of LOF porosity, voids, and cracks. These multiple defects appear to act as preferential sites for localized corrosion, resulting in a decreased pitting potential (E_{pit}) and influencing the repassivation potential (E_{rep}) as depicted in **Fig. 4.5**. This finding underscores the importance of considering the cumulative effect of multiple defects, including LOF porosity, voids, and cracks, on the pitting corrosion behavior of the material.

Following the CPP test, the samples underwent analysis using a light optical microscope (LOM) to identify and quantify the porosity acting as a preferential site for localized corrosion. Purple arrows were used to highlight the porosity in **Fig. 4.4**. This targeted quantification of the porous areas actively involved in pitting propagation offers valuable insights into the specific impact of porosity on pitting corrosion.

Type	Before trial	After trial	Pit Morphology
Wrought 316L SS	<p>(a)</p> 	<p>(f)</p> 	<p>(k)</p> 
316L SS-LPBF Defect: Microcracks PS3.2	<p>(b)</p> 	<p>(g)</p> 	<p>(l)</p> 

Continued

Continued from previous page.

Type	Before trial	After trial	Pit Morphology
316L SS-LPBF Defect: LOF PS3.9	(c) 	(h) 	(m) 



Continued

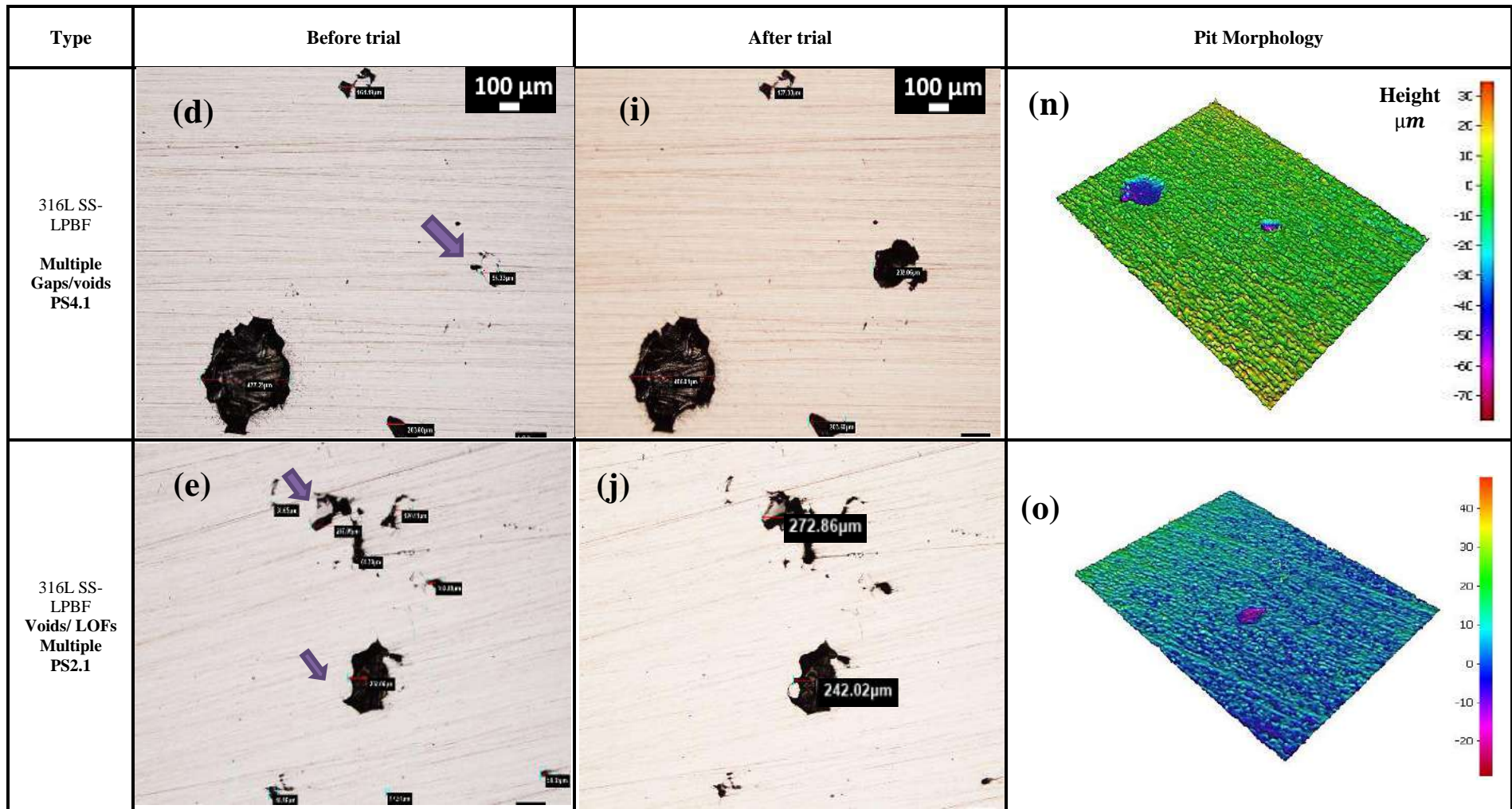


Fig. 4.4 The morphology of the wrought and 316L stainless steel (316L SS) LPBF specimens before and after the test. The figure provides visual representations of the specimen surfaces, illustrating any changes in morphology due to the testing process. The comparison between the pre-test (a-b) and post-test (f-j) and images of the pit (k-o) allows for a better understanding of the structural alterations that occurred during the testing of LPBF specimens.

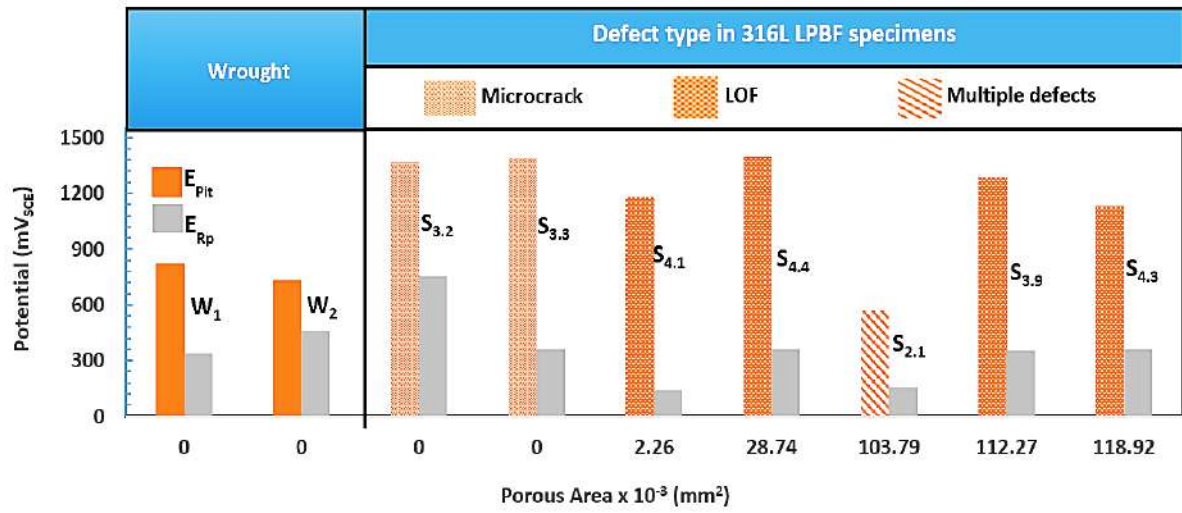


Fig. 4.5 Correlation between potential values and porous area in tested specimens

CHAPTER 5

5. DISCUSSIONS

The pitting potentials measured through the CPP are the potentials above which stable pitting propagation occurs. As indicated by many researchers, the occurrence of stable pitting requires the maintaining of sufficiently aggressive local chemistry inside the pit cavity [23]–[25]. Galvele [74] firstly introduced the concept of the pit stability product (xi), which is the product of current density, i , and pit depth, x , to indicate the aggressiveness of the local chemistry. When the pit stability product is above the critical value [4], [26], [28], [29], the sufficiently aggressive local chemistry can be maintained inside the pit cavity, thus pit can propagate or grow stably [74].

It is understandable that the porosity would not influence the critical pit stability product, which is only related with the material composition, temperature and exposing environment. This study identifies microcracks as favorable sites for stable pitting corrosion. The microcracks could facilitate the accumulation of the metal cations during the CPP tests. Compared with the defect-free surface, microcracks led to a higher x for the same critical pit stability product, thus a lower current density and pitting potential was expected for microcracks. Thus microcracks served as the preferential site for stable pitting propagation. This finding aligns with the established pitting corrosion framework [17], [18], [20]–[22].

The study also highlights the role of LOF defects in pitting corrosion. LOFs play a significant role in pitting corrosion by acting as preferred sites for initiation and propagation. Similar with the microcracks, LOF porosity led to a higher x for the same critical pit stability product, thus LOF was expected to be the preferential stable pitting propagation location. As indicated, the equivalent x for microcracks and different size LOF could be similar, thus the pitting potentials was not significantly by the presence of LOF as well as the size of LOF.

While previous studies have explored the influence of LOF defects on localized corrosion and the formation of corrosion pits [2], [6], their focus has predominantly been on assessing the overall percentage of defects in the specimens. This study stands apart by taking a more targeted approach, quantifying and analyzing only the porosity that actively contributes to pitting corrosion.

Furthermore, the presence of multiple defects decreases pitting potentials, indicating a higher susceptibility to pitting corrosion. These defects serve as initiation points for corrosive attack, increasing the likelihood of pit formation and ultimately lowering overall pitting potential. However, open porosity does not contribute to pitting propagation, emphasizing the importance of intricate defects in samples with multiple defects. Further investigation is needed to fully understand the mechanism behind this phenomenon.

Gas voids, on the other hand, exhibit limited impact on pitting corrosion due to their open geometry [4]. The shape of gas voids allows for the dissipation of ion concentration preventing the accumulation of metal cations within the pore. Thus the gas voids should behave similarly with the defect-free surface.

Additionally, the strengths of this study are the use of an enhanced syringe cell incorporating a metal bridge, which greatly enhances the reliability of the outcomes by providing more robust data. By focusing on quantifying only the porous that actively participate in pitting propagation, the study offers valuable insights into the specific impact of porosity on pitting corrosion. This targeted approach improves the understanding of the complex relationship between porosity and pitting corrosion. Moreover, the use of cyclic potentiodynamic polarization testing, coupled with a comprehensive comparison to existing literature, further bolsters the reliability and validity of the findings.

However, certain limitations should be acknowledged and addressed in future studies. The monitoring of the syringe method, although improved by the metal bridge, could benefit

from further enhancements to ensure precise and accurate measurements. Exploring the adoption of an automatic pipette as an alternative method could enhance control and reproducibility in future experiments, contributing to the overall improvement of data quality.

To further improve the outcomes of this investigation, several strategies can be considered. Firstly, increasing the sample size and expanding the range of LPBF 316L stainless steel specimens with varying defect characteristics would provide a more comprehensive understanding of the pitting corrosion behavior. Additionally, conducting long-term exposure tests under realistic operating conditions could reveal the performance of LPBF-fabricated components over extended periods.

Furthermore, investigating the influence of different process parameters on the formation and severity of defects, such as porosity and LOF, would offer valuable insights into process optimization and defect mitigation strategies. Additionally, implementing advanced characterization techniques, such as electron microscopy and X-ray tomography, could provide more detailed information on defect morphology and distribution, aiding in the interpretation of pitting corrosion mechanisms.

Collaborating with multidisciplinary experts in corrosion science and materials engineering would also be beneficial, as their insights and expertise could contribute to the development of innovative solutions for enhancing the pitting corrosion resistance of LPBF-fabricated components. Finally, conducting field studies and evaluating the performance of LPBF components in real-world applications would provide valuable feedback and validation of the laboratory findings.

CHAPTER 6

6. CONCLUSIONS

In this study, the influence of various defects on the pitting corrosion behavior of LPBF-fabricated 316L SS specimens was investigated using cyclic potentiodynamic polarization in a 0.6M NaCl. Thus, the findings from this investigation provide valuable insights allowing draft the following conclusions:

- Although pit propagation could occur from micro cracks, the pitting resistance of LPBF 316L SS was superior to its wrought counterpart. This indicates that despite the presence of micro cracks, the LPBF fabrication process still offers advantages in terms of pitting corrosion resistance.
- Gas voids were not the preferred sites for pitting propagation. The presence of voids with their open porosity cannot accelerate the accumulation of metal cations.
- On the other hand, LOF defects and microcracks, specifically, served as the preferred sites for pitting initiation and propagation. However, the size of LOF did not significantly influence the pitting resistance.
- The presence of multiple defects significantly decreased the pitting potentials. Further research is needed to explore the mechanism.

In conclusion, this study significantly advances the understanding of pitting corrosion behavior in LPBF 316L stainless steel and sheds light on the role of different defects. The findings emphasize the importance of considering the presence of microcracks and LOF defects in the design and optimization of LPBF-fabricated components to enhance their resistance to pitting corrosion. Moving forward, future research endeavors should prioritize the development of strategies to mitigate the impact of defects and further investigate the underlying mechanisms, aiming for more effective corrosion control in LPBF applications.

REFERENCES

- [1] M. Gor *et al.*, “A Critical Review on Effect of Process Parameters on Mechanical and Microstructural Properties of Powder-Bed Fusion Additive Manufacturing of SS316L,” *Materials (Basel)*, vol. 14, no. 21, p. 6527, Oct. 2021, doi: 10.3390/ma14216527.
- [2] M. Laleh *et al.*, “Two and three-dimensional characterisation of localised corrosion affected by lack-of-fusion pores in 316L stainless steel produced by selective laser melting,” *Corros. Sci.*, vol. 165, no. September 2019, p. 108394, Apr. 2020, doi: 10.1016/j.corsci.2019.108394.
- [3] G. Sander *et al.*, “On The Corrosion and Metastable Pitting Characteristics of 316L Stainless Steel Produced by Selective Laser Melting,” *J. Electrochem. Soc.*, vol. 164, no. 6, pp. C250–C257, Mar. 2017, doi: 10.1149/2.0551706jes.
- [4] Z. Duan *et al.*, “Pitting behavior of SLM 316L stainless steel exposed to chloride environments with different aggressiveness: Pitting mechanism induced by gas pores,” *Corros. Sci.*, vol. 167, no. September 2019, p. 108520, 2020, doi: 10.1016/j.corsci.2020.108520.
- [5] Y. Zhang, F. Liu, J. Chen, and Y. Yuan, “Effects of surface quality on corrosion resistance of 316L stainless steel parts manufactured via SLM,” *J. Laser Appl.*, vol. 29, no. 2, p. 022306, May 2017, doi: 10.2351/1.4983263.
- [6] Z. Zhang, X. Yuan, Z. Zhao, X. Li, B. Liu, and P. Bai, “Electrochemical noise comparative study of pitting corrosion of 316L stainless steel fabricated by selective laser melting and wrought,” *J. Electroanal. Chem.*, vol. 894, no. February, p. 115351, Aug. 2021, doi: 10.1016/j.jelechem.2021.115351.
- [7] Y. Sun, A. Moroz, and K. Alrbaey, “Sliding Wear Characteristics and Corrosion Behaviour of Selective Laser Melted 316L Stainless Steel,” *J. Mater. Eng. Perform.*, vol. 23, no. 2, pp. 518–526, Feb. 2014, doi: 10.1007/s11665-013-0784-8.
- [8] V. B. Vukkum and R. K. Gupta, “Review on corrosion performance of laser powder-bed fusion printed 316L stainless steel: Effect of processing parameters, manufacturing defects, post-processing, feedstock, and microstructure,” *Mater. Des.*, vol. 221, p. 110874, Sep. 2022, doi: 10.1016/j.matdes.2022.110874.
- [9] W. H. Kan *et al.*, “A critical review on the effects of process-induced porosity on the mechanical properties of alloys fabricated by laser powder bed fusion,” *J. Mater. Sci.*, vol. 57, no. 21, pp. 9818–9865, Jun. 2022, doi: 10.1007/s10853-022-06990-7.
- [10] T. Voisin *et al.*, “Pitting Corrosion in 316L Stainless Steel Fabricated by Laser Powder Bed Fusion Additive Manufacturing: A Review and Perspective,” *JOM*, vol. 74, no. 4, pp. 1668–1689, Apr. 2022, doi: 10.1007/s11837-022-05206-2.
- [11] E. Li, Z. Zhou, L. Wang, H. Shen, R. Zou, and A. Yu, “Particle scale modelling of melt pool dynamics and pore formation in selective laser melting additive manufacturing,” *Powder Technol.*, vol. 397, p. 117012, Jan. 2022, doi: 10.1016/j.powtec.2021.11.056.
- [12] J. A. Cherry, H. M. Davies, S. Mehmood, N. P. Lavery, S. G. R. Brown, and J. Sienz, “Investigation into the effect of process parameters on microstructural and physical properties of 316L stainless steel parts by selective laser melting,” *Int. J. Adv. Manuf. Technol.*, vol. 76, no. 5–8, pp. 869–879, 2015, doi: 10.1007/s00170-014-6297-2.
- [13] Z. Sun, X. Tan, S. B. Tor, and W. Y. Yeong, “Selective laser melting of stainless steel 316L with low porosity and high build rates,” *Mater. Des.*, vol. 104, pp. 197–204, 2016, doi: 10.1016/j.matdes.2016.05.035.
- [14] X. Lou, M. Song, P. W. Emigh, M. A. Othon, and P. L. Andresen, “On the stress corrosion crack growth behaviour in high temperature water of 316L stainless steel made by laser powder bed fusion additive manufacturing,” *Corros. Sci.*, vol. 128, no. February, pp. 140–153, Nov. 2017, doi: 10.1016/j.corsci.2017.09.017.
- [15] M. Ziętała *et al.*, “The microstructure, mechanical properties and corrosion resistance of 316L stainless steel fabricated using laser engineered net shaping,” *Mater. Sci. Eng. A*, vol. 677, pp. 1–10, Nov. 2016, doi: 10.1016/j.msea.2016.09.028.
- [16] W. S. W. Harun, R. I. M. Asri, F. R. M. Romlay, S. Sharif, N. H. M. Jan, and F. Tsumori, “Surface characterisation and corrosion behaviour of oxide layer for SLMed-316L stainless steel,” *J. Alloys Compd.*, vol. 748, pp. 1044–1052, Jun. 2018, doi: 10.1016/j.jallcom.2018.03.233.
- [17] G. S. Frankel, “Pitting Corrosion of Metals: A Review of the Critical Factors,” *J. Electrochem. Soc.*, vol. 145, no. 6, pp. 2186–2198, 1998, doi: 10.1149/1.1838615.
- [18] D. D. Macdonald, “The history of the Point Defect Model for the passive state: A brief review of film growth aspects,” *Electrochim. Acta*, vol. 56, no. 4, pp. 1761–1772, Jan. 2011, doi: 10.1016/j.electacta.2010.11.005.
- [19] Y. Zuo, H. Wang, and J. Xiong, “The aspect ratio of surface grooves and metastable pitting of stainless steel,” *Corros. Sci.*, vol. 44, no. 1, pp. 25–35, 2002, doi: 10.1016/S0010-938X(01)00039-7.
- [20] D. D. Macdonald, “Passivity: Enabler of our metals based civilisation,” *Corros. Eng. Sci. Technol.*, vol. 49, no. 2, pp. 143–155, 2014, doi: 10.1179/1743278214Y.0000000158.
- [21] K. M. Emran and H. Al-Refai, “Resistivity and passivity characterization of Ni-base glassy alloys in NaOH media,” *Metals (Basel)*, vol. 8, no. 1, 2018, doi: 10.3390/met8010064.
- [22] P. C. Pistorius and G. T. Burstein, “Metastable pitting corrosion of stainless steel and the transition to stability,” *Philos. Trans. R. Soc. London. Ser. A Phys. Eng. Sci.*, vol. 341, no. 1662, pp. 531–559, Dec. 1992, doi: 10.1098/rsta.1992.0114.
- [23] G. S. Frankel, T. Li, and J. R. Scully, “Perspective—Localized Corrosion: Passive Film Breakdown vs Pit Growth Stability,” *J. Electrochem. Soc.*, vol. 164, no. 4, pp. C180–C181, 2017, doi: 10.1149/2.1381704jes.
- [24] T. Li, J. R. Scully, and G. S. Frankel, “Localized Corrosion: Passive Film Breakdown vs Pit Growth Stability: Part II. A Model for Critical Pitting Temperature,” *J. Electrochem. Soc.*, vol. 165, no. 9, pp. C484–C491, 2018, doi: 10.1149/2.0591809jes.
- [25] T. Li, J. Wu, and G. S. Frankel, “Localized corrosion: Passive film breakdown vs. Pit growth stability. Part VI: Pit dissolution kinetics of different alloys and a model for pitting and repassivation potentials,” *Corros. Sci.*, vol. 182, no. November 2020, p. 109277, Apr. 2021, doi: 10.1016/j.corsci.2021.109277.
- [26] M. G. Fontana, *Corrosion Engineering And Corrosion Science*, vol. 19, no. 6. 1963. doi: 10.5006/0010-9312-19.6.199.
- [27] T. Li, J. R. Scully, and G. S. Frankel, “Localized Corrosion: Passive Film Breakdown vs. Pit Growth Stability: Part III. A Unifying Set of Principal Parameters and Criteria for Pit Stabilization and Salt Film Formation,” *J. Electrochem. Soc.*, vol. 165, no. 11, pp. C762–C770, Aug. 2018, doi: 10.1149/2.0251811jes.
- [28] C. Man, C. Dong, J. Liang, K. Xiao, Q. Yu, and X. Li, “Characterization of the Passive Film and Corrosion of Martensitic AM355 Stainless Steel,” *Anal. Lett.*, vol. 50, no. 7, pp. 1091–1111, 2017, doi: 10.1080/00032719.2016.1210617.
- [29] Z. Cui *et al.*, “Passivation behavior and surface chemistry of 2507 super duplex stainless steel in artificial seawater: Influence of dissolved oxygen and pH,” *Corros. Sci.*, vol. 150, no. December 2018, pp. 218–234, Apr. 2019, doi:

- 10.1016/j.corsci.2019.02.002.
- [30] Q. Chao *et al.*, “On the enhanced corrosion resistance of a selective laser melted austenitic stainless steel,” *Scr. Mater.*, vol. 141, pp. 94–98, 2017, doi: 10.1016/j.scriptamat.2017.07.037.
- [31] J. Nie, L. Wei, Y. Jiang, Q. Li, and H. Luo, “Corrosion mechanism of additively manufactured 316 L stainless steel in 3.5 wt.% NaCl solution,” *Mater. Today Commun.*, vol. 26, p. 101648, Mar. 2021, doi: 10.1016/j.mtcomm.2020.101648.
- [32] V. B. Vukkum, J. Christudasjustus, A. A. Darwish, S. M. Storck, and R. K. Gupta, “Enhanced corrosion resistance of additively manufactured stainless steel by modification of feedstock,” *npj Mater. Degrad.*, vol. 6, no. 1, p. 2, Dec. 2022, doi: 10.1038/s41529-021-00215-z.
- [33] J. R. Trelewicz, G. P. Halada, O. K. Donaldson, and G. Manogharan, “Microstructure and Corrosion Resistance of Laser Additively Manufactured 316L Stainless Steel,” *JOM*, vol. 68, no. 3, pp. 850–859, Mar. 2016, doi: 10.1007/s11837-016-1822-4.
- [34] D. Kong *et al.*, “Mechanical properties and corrosion behavior of selective laser melted 316L stainless steel after different heat treatment processes,” *J. Mater. Sci. Technol.*, vol. 35, no. 7, pp. 1499–1507, Jul. 2019, doi: 10.1016/j.jmst.2019.03.003.
- [35] A. B. Kale, B.-K. Kim, D.-I. Kim, E. G. Castle, M. Reece, and S.-H. Choi, “An investigation of the corrosion behavior of 316L stainless steel fabricated by SLM and SPS techniques,” *Mater. Charact.*, vol. 163, no. February, p. 110204, May 2020, doi: 10.1016/j.matchar.2020.110204.
- [36] G. Sander, D. Jiang, Y. Wu, and N. Birbilis, “Exploring the possibility of a stainless steel and glass composite produced by additive manufacturing,” *Mater. Des.*, vol. 196, p. 109179, Nov. 2020, doi: 10.1016/j.matdes.2020.109179.
- [37] C. Man, C. Dong, T. Liu, D. Kong, D. Wang, and X. Li, “The enhancement of microstructure on the passive and pitting behaviors of selective laser melting 316L SS in simulated body fluid,” *Appl. Surf. Sci.*, vol. 467–468, no. October 2018, pp. 193–205, Feb. 2019, doi: 10.1016/j.apsusc.2018.10.150.
- [38] G. Wang, Q. Liu, H. Rao, H. Liu, and C. Qiu, “Influence of porosity and microstructure on mechanical and corrosion properties of a selectively laser melted stainless steel,” *J. Alloys Compd.*, vol. 831, p. 154815, Aug. 2020, doi: 10.1016/j.jallcom.2020.154815.
- [39] Y. Ait Albrimi, A. Eddib, J. Douch, Y. Berghoute, M. Hamdani, and R. M. Souto, “Electrochemical behaviour of AISI 316 austenitic stainless steel in acidic media containing chloride ions,” *Int. J. Electrochem. Sci.*, vol. 6, no. 10, pp. 4614–4627, 2011.
- [40] A. Robin, G. Silva, and J. L. Rosa, “Corrosion behavior of HA-316L SS biocomposites in aqueous solutions,” *Mater. Res.*, vol. 16, no. 6, pp. 1254–1259, Aug. 2013, doi: 10.1590/S1516-14392013005000136.
- [41] Z. Szklarska-Smialowska and J. Mankowski, “Crevice corrosion of stainless steels in sodium chloride solution,” *Corros. Sci.*, vol. 18, no. 11, pp. 953–960, Jan. 1978, doi: 10.1016/0010-938X(78)90030-6.
- [42] S. M. Sharland, “A review of the theoretical modelling of crevice and pitting corrosion,” *Corros. Sci.*, vol. 27, no. 3, pp. 289–323, Jan. 1987, doi: 10.1016/0010-938X(87)90024-2.
- [43] R. Jeffrey and R. E. Melchers, “Effect of Vertical Length on Corrosion of Steel in the Tidal Zone,” *CORROSION*, vol. 65, no. 10, pp. 695–702, Oct. 2009, doi: 10.5006/1.3319096.
- [44] J. Zhang, J. Yuan, Y. Qiao, C. Cao, J. Zhang, and G. Zhou, “The corrosion and passivation of SS304 stainless steel under square wave electric field,” *Mater. Chem. Phys.*, vol. 79, no. 1, pp. 43–48, Mar. 2003, doi: 10.1016/S0254-0584(02)00445-5.
- [45] N. Birbilis, B. N. Padgett, and R. G. Buchheit, “Limitations in microelectrochemical capillary cell testing and transformation of electrochemical transients for acquisition of microcell impedance data,” *Electrochim. Acta*, vol. 50, no. 16–17, pp. 3536–3544, May 2005, doi: 10.1016/j.electacta.2005.01.010.
- [46] F. Arjmand and A. Adriaens, “Microcapillary electrochemical droplet cells: applications in solid-state surface analysis,” *J. Solid State Electrochem.*, vol. 18, no. 7, pp. 1779–1788, Jul. 2014, doi: 10.1007/s10008-014-2413-3.
- [47] J. Shen, G. Song, D. Zheng, and Z. Wang, “A double-mode cell to measure pitting and crevice corrosion,” *Mater. Corros.*, vol. 70, no. 12, pp. 2228–2237, Dec. 2019, doi: 10.1002/maco.201910932.
- [48] A. M. Panindre, K. H. Chang, T. Weirich, and G. S. Frankel, “Technical note: Syringe cell for electrochemical testing,” *Corrosion*, vol. 74, no. 8, pp. 847–850, 2018, doi: 10.5006/2847.
- [49] S. Choudhary, K. Marusak, T. Eldred, and R. G. Kelly, “Use of a Bipolar, Metallic Luggin-Haber Probe for Electrochemical Measurements of Interfacial Potential,” *J. Electrochem. Soc.*, vol. 169, no. 11, p. 111505, Nov. 2022, doi: 10.1149/1945-7111/aca367.
- [50] K. Saeidi, X. Gao, Y. Zhong, and Z. J. Shen, “Hardened austenite steel with columnar sub-grain structure formed by laser melting,” *Mater. Sci. Eng. A*, vol. 625, pp. 221–229, Feb. 2015, doi: 10.1016/j.msea.2014.12.018.
- [51] K. Wang *et al.*, “On the pitting behaviour of laser powder bed fusion prepared 316L stainless steel upon post-processing heat treatments,” *Corros. Sci.*, vol. 197, no. September 2021, p. 110060, Apr. 2022, doi: 10.1016/j.corsci.2021.110060.
- [52] B. M. Morrow *et al.*, “Impact of Defects in Powder Feedstock Materials on Microstructure of 304L and 316L Stainless Steel Produced by Additive Manufacturing,” *Metall. Mater. Trans. A*, vol. 49, no. 8, pp. 3637–3650, Aug. 2018, doi: 10.1007/s11661-018-4661-9.
- [53] M. J. Heiden *et al.*, “Evolution of 316L stainless steel feedstock due to laser powder bed fusion process,” *Addit. Manuf.*, vol. 25, no. November 2018, pp. 84–103, Jan. 2019, doi: 10.1016/j.addma.2018.10.019.
- [54] Y. Shi, Z. Li, H. Sun, S. Huang, and F. Zeng, “Effect of the properties of the polymer materials on the quality of selective laser sintering parts,” *Proc. I MECH E Part L J. Mater. Appl.*, vol. 218, no. 3, pp. 247–252, Aug. 2004, doi: 10.1243/1464420041579454.
- [55] N. Shamsaei, A. Yadollahi, L. Bian, and S. M. Thompson, “An overview of Direct Laser Deposition for additive manufacturing: Part II: Mechanical behavior, process parameter optimization and control,” *Addit. Manuf.*, vol. 8, pp. 12–35, Oct. 2015, doi: 10.1016/j.addma.2015.07.002.
- [56] C. Pazon, E. Hryha, P. Forêt, and L. Nyborg, “Effect of argon and nitrogen atmospheres on the properties of stainless steel 316 L parts produced by laser-powder bed fusion,” *Mater. Des.*, vol. 179, p. 107873, Oct. 2019, doi: 10.1016/j.matdes.2019.107873.
- [57] D.-R. Eo, S. G. Chung, J. M. Jeon, and J.-W. Cho, “Melt pool oxidation and reduction in powder bed fusion,” *Addit. Manuf.*, vol. 41, no. October 2020, p. 101982, May 2021, doi: 10.1016/j.addma.2021.101982.
- [58] A. Elias, A. Czekanski, and S. Boakye-Yiadom, “Effect of laser powder bed fusion parameters on the microstructural evolution and hardness of 316L stainless steel,” *Int. J. Adv. Manuf. Technol.*, vol. 113, no. 9–10, pp. 2651–2669, Apr. 2021, doi:

- 10.1007/s00170-021-06818-9.
- [59] G. Sander *et al.*, “Corrosion of Additively Manufactured Alloys: A Review,” *CORROSION*, vol. 74, no. 12, pp. 1318–1350, Dec. 2018, doi: 10.5006/2926.
- [60] J. Liu *et al.*, “Effect of scanning speed on the microstructure and mechanical behavior of 316L stainless steel fabricated by selective laser melting,” *Mater. Des.*, vol. 186, p. 108355, Jan. 2020, doi: 10.1016/j.matdes.2019.108355.
- [61] R. Li, J. Liu, Y. Shi, M. Du, and Z. Xie, “316L stainless steel with gradient porosity fabricated by selective laser melting,” *J. Mater. Eng. Perform.*, vol. 19, no. 5, pp. 666–671, 2010, doi: 10.1007/s11665-009-9535-2.
- [62] Y. Shang, Y. Yuan, D. Li, Y. Li, and J. Chen, “Effects of scanning speed on in vitro biocompatibility of 316L stainless steel parts elaborated by selective laser melting,” *Int. J. Adv. Manuf. Technol.*, vol. 92, no. 9–12, pp. 4379–4385, Oct. 2017, doi: 10.1007/s00170-017-0525-5.
- [63] A. T. Sutton, C. S. Kriewall, M. C. Leu, and J. W. Newkirk, “Powder characterisation techniques and effects of powder characteristics on part properties in powder-bed fusion processes,” *Virtual Phys. Prototyp.*, vol. 12, no. 1, pp. 3–29, Jan. 2017, doi: 10.1080/17452759.2016.1250605.
- [64] H. Jia, H. Sun, H. Wang, Y. Wu, and H. Wang, “Scanning strategy in selective laser melting (SLM): a review,” *Int. J. Adv. Manuf. Technol.*, vol. 113, no. 9–10, pp. 2413–2435, 2021, doi: 10.1007/s00170-021-06810-3.
- [65] T. Voisin *et al.*, “New insights on cellular structures strengthening mechanisms and thermal stability of an austenitic stainless steel fabricated by laser powder-bed-fusion,” *Acta Mater.*, vol. 203, p. 116476, Jan. 2021, doi: 10.1016/j.actamat.2020.11.018.
- [66] G. Sander, A. P. Babu, X. Gao, D. Jiang, and N. Birbilis, “On the effect of build orientation and residual stress on the corrosion of 316L stainless steel prepared by selective laser melting,” *Corros. Sci.*, vol. 179, p. 109149, Feb. 2021, doi: 10.1016/j.corsci.2020.109149.
- [67] M. J. Paul *et al.*, “Fracture resistance of AlSi10Mg fabricated by laser powder bed fusion,” *Acta Mater.*, vol. 211, p. 116869, Jun. 2021, doi: 10.1016/j.actamat.2021.116869.
- [68] R. Li, Y. Shi, Z. Wang, L. Wang, J. Liu, and W. Jiang, “Densification behavior of gas and water atomized 316L stainless steel powder during selective laser melting,” *Appl. Surf. Sci.*, vol. 256, no. 13, pp. 4350–4356, Apr. 2010, doi: 10.1016/j.apsusc.2010.02.030.
- [69] D. Wang, Y. Liu, Y. Yang, and D. Xiao, “Theoretical and experimental study on surface roughness of 316L stainless steel metal parts obtained through selective laser melting,” *Rapid Prototyp. J.*, vol. 22, no. 4, pp. 706–716, Jun. 2016, doi: 10.1108/RPJ-06-2015-0078.
- [70] E. Liverani, S. Toschi, L. Ceschini, and A. Fortunato, “Effect of selective laser melting (SLM) process parameters on microstructure and mechanical properties of 316L austenitic stainless steel,” *J. Mater. Process. Technol.*, vol. 249, no. November 2016, pp. 255–263, Nov. 2017, doi: 10.1016/j.jmatprotec.2017.05.042.
- [71] L. Hao, S. Dadbakhsh, O. Seaman, and M. Felstead, “Selective laser melting of a stainless steel and hydroxyapatite composite for load-bearing implant development,” *J. Mater. Process. Technol.*, vol. 209, no. 17, pp. 5793–5801, Aug. 2009, doi: 10.1016/j.jmatprotec.2009.06.012.
- [72] D. Xia *et al.*, “A mechanistic study on thiosulfate-enhanced passivity degradation of Alloy 800 in chloride solutions,” *Electrochim. Acta*, vol. 111, pp. 510–525, Nov. 2013, doi: 10.1016/j.electacta.2013.08.030.
- [73] H. Wang, J. Xie, K. P. Yan, M. Duan, and Y. Zuo, “The nucleation and growth of metastable pitting on pure iron,” *Corros. Sci.*, vol. 51, no. 1, pp. 181–185, Jan. 2009, doi: 10.1016/j.corsci.2008.09.024.
- [74] J. R. Galvele, “Transport Processes and the Mechanism of Pitting of Metals,” *J. Electrochem. Soc.*, vol. 123, no. 4, pp. 464–474, Apr. 1976, doi: 10.1149/1.2132857.

Appendix A: A photograph of the syringe cell configuration and data obtained in the experiments.

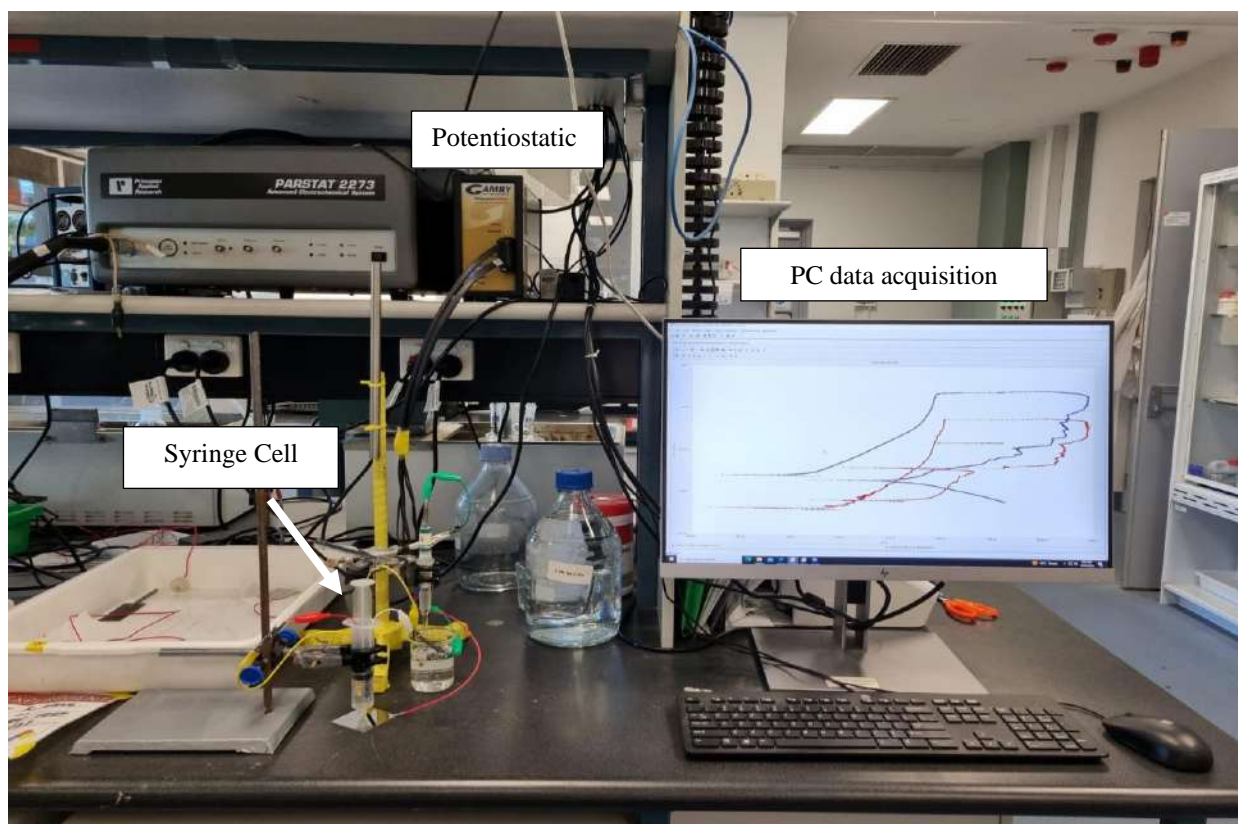


Fig. 6.1 Syringe cell configuration located in the laboratory of Curtin Corrosion Centre.

Table 6.1 Data obtained through the experiments.

Area porosity mm ²	E _{pit} (mV vs. SSE)	E _{rp} (mV vs. SSE)	Name Sample	Type of defect
0	823	339	WS1	no defect
0	732.2	462	WS2	no defect
0	1369	754	PS3.2	micro cracks
0	1390	357	PS3.3	micro cracks
2.26	1181	144	PS4.1	LOF
28.74	1397	357	PS4.4	LOF
103.79	569	157	PS2.1	Multiple
112.27	1285	356	PS3.9	LOF
118.92	1130	362	PS4.3	LOF